

Catalysis Science & Technology

Accepted Manuscript

This article can be cited before page numbers have been issued, to do this please use: V. Marchuk, X. Huang, J. Grunwaldt and D. E. Doronkin, *Catal. Sci. Technol.*, 2023, DOI: 10.1039/D2CY02095E.



This is an Accepted Manuscript, which has been through the Royal Society of Chemistry peer review process and has been accepted for publication.

Accepted Manuscripts are published online shortly after acceptance, before technical editing, formatting and proof reading. Using this free service, authors can make their results available to the community, in citable form, before we publish the edited article. We will replace this Accepted Manuscript with the edited and formatted Advance Article as soon as it is available.

You can find more information about Accepted Manuscripts in the [Information for Authors](#).

Please note that technical editing may introduce minor changes to the text and/or graphics, which may alter content. The journal's standard [Terms & Conditions](#) and the [Ethical guidelines](#) still apply. In no event shall the Royal Society of Chemistry be held responsible for any errors or omissions in this Accepted Manuscript or any consequences arising from the use of any information it contains.

ARTICLE

Structure sensitivity of alumina- and zeolite-supported platinum ammonia slip catalysts

Vasyl Marchuk,^a Xiaohui Huang,^{b,c} Jan-Dierk Grunwaldt,^{a,d} and Dmitry E. Doronkin^{*a,d}Received 00th January 20xx,
Accepted 00th January 20xx

DOI: 10.1039/x0xx00000x

The influence of size and structure of Pt particles on the catalytic performance in selective ammonia oxidation for emission control applications is hardly understood. There is a lack of *in situ* structural characterization to explain catalyst performance under atmospheric pressure and relevant reactant ratios. In this study we complemented conventional laboratory tests with *operando* X-ray absorption spectroscopy (XAS) to determine activity- and selectivity-governing factors in ammonia slip catalysts with different Pt particle sizes supported on γ -alumina and a ZSM-5 zeolite. A previously reported narrow activity range of platinum catalysts was extended by using catalysts with atomically and sub-nanometre dispersed Pt. The increase in activity with particle size was mainly caused by the availability of favourable Pt ensembles on the surface, probably B5 sites. Below the required size for existence of these ensembles (~ 2 nm) Pt possessed poor activity for ammonia oxidation, while upon reaching it the activity drastically rose and was further moderately dependent on particle size. Spectroscopic data revealed the same reaction mechanism for particles ≥ 2 nm. It included initial reduction during heating in reaction mixture and subsequent re-oxidation at high temperatures. For Pt single sites / small clusters, the mechanism was different and involved only gradual reduction without further re-oxidation. The individual spectral components for the two types of mechanisms were resolved. Their evolution correlated with catalysts activity and selectivity change. While ammonia oxidation proceeded through Ostwald mechanism on active catalysts with sufficiently large particles, single or low-coordinated sites were rather likely to catalyse selective catalytic reduction.

Introduction

Ammonia is regarded as a potential carbon-free energy carrier of the future.¹ It has high energy density, can be easily liquefied and transported through a well-developed infrastructure, which can make it an important component of transition to sustainable economy.²⁻⁴ To regain the energy stored in ammonia, it can be split to hydrogen, used in fuel cells or directly combusted.^{4,5} During these processes ammonia slip will inevitably occur. Since it is a toxic and environmentally harmful gas, ammonia abatement is required. An effective way to accomplish this is using ammonia slip catalysts (ASCs) that selectively oxidise ammonia to harmless nitrogen and water.^{6,7} Ammonia slip catalysts are also widely used in automotive industry to eliminate residual ammonia that is overstoichiometrically dosed for selective catalytic reduction (SCR) of NO_x that are formed during fuel combustion.^{8,9} ASCs

usually combine oxidation functionality, typically a supported Pt catalyst, with SCR functionally, often provided by zeolite-supported Fe or Cu.^{8,10} Due to rising noble metal prices it is important to optimise the content of platinum in ASCs increasing its activity while decreasing the loading. Another issue of platinum catalysts is that, despite sufficient activity at low temperatures (< 200 °C), they demonstrate low selectivity to nitrogen at increased temperatures (> 300 °C) producing high amounts of N₂O or NO_x.¹¹⁻¹³ To solve these problems and to improve the performance of ASCs, understanding the structure of a catalyst and its relation to activity and selectivity is required.

Many studies that detect catalyst structure and directly correlate it with its performance apply model reaction conditions, such as vacuum or unsupported Pt in a form of single crystals, foil or wires.¹⁴⁻²⁰ On the other hand, the studies of more realistic systems with supported Pt under atmospheric pressure were conducted.^{13,18,21,22} These works mostly characterise the state of Pt either before or after the reaction. It is necessary to probe the catalyst also during operation since its state might drastically vary under reaction conditions.^{23,24}

A number of studies addressed the topic of the structure sensitivity of ammonia oxidation inspecting ASCs with different particle sizes. This approach is well-established in unravelling structure-activity relationships, since particles of different sizes often expose different groups of surface atoms with varying coordination and oxidation states and thus with different activity.²⁵ For example, earlier works by Ostermaier et al.^{26,27}

^a Institute for Chemical Technology and Polymer Chemistry (ITCP), Karlsruhe Institute of Technology, Engesserstr. 20, 76131, Karlsruhe, Germany.

^b Institute of Nanotechnology (INT), Karlsruhe Institute of Technology, Hermann-von-Helmholtz-Platz 1, 76344, Eggenstein-Leopoldshafen, Germany.

^c Department of Materials and Earth Sciences, Technische Universität Darmstadt, Alarich-Weiss-Straße 2, 64287, Darmstadt, Germany.

^d Institute of Catalysis Research and Technology (IKFT), Karlsruhe Institute of Technology, Hermann-von-Helmholtz-Platz 1, 76344, Eggenstein-Leopoldshafen, Germany. E-mail: dmitry.doronkin@kit.edu

Electronic Supplementary Information (ESI) available: *ex situ* XANES and EXAFS spectra, and the corresponding fits, HAADF-STEM images, additional catalytic data, Arrhenius plots and TOF calculations, additional *operando* XANES data. See DOI: 10.1039/x0xx00000x



and van den Broek^{28, 29} have already reported an increase of the reaction rate with growth of Pt particle size. However, the conditions applied in these works did not completely correspond to the conditions present in emission control systems. In particular, Ostermaier et al. used a narrow temperature range (120–200 °C). In the case of van den Broek too low O₂ partial pressures were used. These points were taken into account in the following studies, and the size effect in ammonia oxidation was thoroughly studied in a Pt nanoparticle range from 1 to 23 nm³⁰ and even for a size range of 1.3–200 nm.³¹ Interestingly, in the latter case, despite the huge size range studied and a realistic gas feed, only a moderate size effect on the activity was observed. The variation of the temperature of 50 % conversion (T_{50%}) did not exceed ~35 °C. Hence, it is important to study the factors which could extend this activity window. According to the present literature, there is only a modest possibility to further lower Pt light-off temperatures by solely increasing its particle size.³¹ Moreover, it is unclear to which extent the light-off temperatures can rise for extremely dispersed Pt. This requires especially particle sizes smaller than 1 nm, which to date have hardly been studied for ASCs.

For understanding the Pt particle size dependence on ammonia oxidation, several factors need to be considered. To explain the structure sensitivity, many experimental studies focus on the varying reducibility of different Pt sites.^{26, 27, 30–34} Various studies conclude that reduced metallic platinum surface is a prerequisite for high ammonia oxidation activity.^{26, 27, 30, 32–34} At the same time, oxygen is stronger bound to step and edge Pt sites, which are more abundant on smaller particles.^{31, 35} As a result, smaller particles are less active for ammonia oxidation. Other studies, many of which are of theoretical nature, claim that the ammonia activation requires a favourable ensemble of surface Pt atoms or presence of terrace steps for the efficient reaction.^{14, 16, 36} The presence of adsorbed oxygen on Pt surface facilitates the activation even more.^{14, 32, 36} This is characteristic for the Ostwald process mechanism that includes stepwise hydrogen subtraction from ammonia by oxygen (O-assisted ammonia dissociation).¹⁶ A certain size of particles related to the specific Pt surface is required for these favourable conditions, typically reported to be ~2 nm.³⁶ In this case, the reaction rate should decline with particle size decrease with an abrupt drop at a point when Pt particle surface is too small to host the adsorbates and intermediates of O-assisted ammonia dissociation. Despite being in line with the observed trends, the concrete experimental evidence at conditions close to real applications of ASCs (i.e. atmospheric pressure, relevant NH₃:O₂ ratio, presence of water) is missing. Furthermore, literature reports of the size effect in ammonia oxidation are lacking *operando* spectroscopic data on the catalyst structure. Applying them would allow to directly correlate catalyst performance with structural changes of platinum catalysts with different Pt particle size. This would promote catalyst development based on rational design rather than on a trial and error approach.

This work aims at studying factors causing Pt structure sensitivity in selective ammonia oxidation reaction by applying

operando XAS. This X-ray technique allows us to track the structure while determining the performance simultaneously at pressures and reactant concentrations close to real applications.^{24, 37–39} In addition to a conventional catalyst series on γ -Al₂O₃, another series was based on ZSM-5 zeolite. Such a comparison has been reported earlier, for example, by Li and Armor²² and van den Broek.²⁹ However, these studies did not show if the support influence remains constant with varying particle sizes of Pt. Additionally, it is unclear how big the difference is between the impacts of support and particle size or how the presence of water might affect the structure-activity relationship. Furthermore, particular attention in this study has been devoted to catalyst series exhibiting a broader range of reaction rates compared to earlier literature reports. This has been attempted by decreasing Pt particle size to values lower than required for the ammonia activation step of the Ostwald process. In this regard, the roles of Pt oxidation state and the minimal surface necessary for ammonia activation have been examined.

Experimental

Catalysts preparation

Three 2 wt. % Pt/Al₂O₃ samples were synthesised through incipient wetness impregnation (IWI). A series of samples with varying Pt particle sizes was prepared by means of thermal treatment of an initial catalyst in air flow.

The PtA-IW sample was the initial catalyst from which the other two in the series were obtained. For its preparation γ -alumina (SASOL SCFa-230, pre-calcined at 750 °C for 4 h in air) was impregnated with a solution of Pt (II) nitrate (Chempur, anhydrous, 99,95 %), dried under air in a fume cupboard for 40 h at room temperature and then for 1 h at 60 °C in static air. The impregnated and dried sample was then calcined at 400 °C (ramp rate 3 °C/min) for 4 h in static air. After calcination the sample was reduced at 400 °C for 2 h in hydrogen flow (5 % H₂, N₂ balance, temperature ramp rate 3 °C/min).

To obtain alumina-supported catalysts with varying particle size, parts of PtA-IW were calcined in air flow for 4 h at 500 °C and 700 °C (ramp rate 5 °C/min in both cases) resulting in samples PtA-IW-500 and PtA-IW-700, respectively.

Additionally, three catalysts on zeolite support were synthesised. For this NH₄-ZSM-5 zeolite was used (Si/Al=11, Clariant). The platinum loading for the zeolite-supported series constituted 1 wt. %. Before preparation, the support was dried at 150 °C for 16 h in static air.

PtZ-IW was synthesised by incipient wetness impregnation of the zeolite using platinum (II) nitrate, anhydrous (Chempur), as a precursor. The impregnated support was dried in air flow at room temperature for 16 h and then additionally at 80 °C for 4 h. The sample was calcined at 500 °C (heating rate – 4 °C/min) in static air for 2 h.

PtZ-IE sample was prepared via ion exchange (IE) following techniques described in literature^{40, 41}. For this the required amount of [Pt(NH₃)₂]Cl₂ (Aldrich, 98 %) for obtaining 1 % Pt



loading on 3 g of the support (51 mg of the precursor) was dissolved in 600 ml of deionized water. Ion exchange was conducted with magnetic stirring at room temperature in ambient atmosphere for 24 h. After that the sample was filtered and rinsed with 800 ml of distilled water. The filtered residue was dried in air flow at room temperature for 16 h and then – for 3.5 h at 80 °C. The dried sample was calcined at 450 °C in air flow for 2 h. The temperature was reached with a slow ramp rate of 0.5 °C/min.

PtZ-IE-R was prepared using the same procedure as PtZ-IE, but with an additional reduction step. The reduction was conducted in 5 % H₂ (N₂ balance) at 400 °C (heating rate 5 °C/min) for 30 min. Pt concentration in PtZ-IE and PtZ-IE-R samples was estimated using the edge jump in the X-ray absorption spectra using impregnated PtZ-IW sample as a reference. The estimated Pt concentration in the ion-exchange samples was 0.9 %. Standard deviation was evaluated on three different zeolite-supported samples obtained through incipient wetness impregnation and constituted 0.17 abs. %. The prepared samples, their abbreviations and their synthesis conditions are summarised in Table 1.

TEM

Powder samples of the synthesised catalysts were directly dispersed on copper grids coated with lacey carbon film (Quantifoil) without use of solvents. High angle annular dark-field (HAADF) scanning transmission electron microscopy (STEM) imaging was performed on a Themis300 transmission electron microscope (ThermoFisher Scientific) equipped with a probe aberration corrector, operating at 300 kV. TEM images were analysed with *ImageJ* software to estimate particle size.⁴²

Catalytic experiments

The catalysts were tested in a plug-flow quartz reactor in a temperature-programmed mode. Three cycles of heating from 50 °C to 400 °C and cooling to 50 °C (ramp rate 3 °C/min, 10 min dwell times) were used. A reaction feed of 500 ppm NH₃, 13 % O₂ in N₂ was used in the first two cycles. In the third cycle, the same NH₃ and O₂ concentrations with additional 5 % H₂O and 10 % CO₂ balanced with N₂ were applied. The first cycle served as catalyst pre-treatment, and the results of the second catalytic cycle are compared in this study for general activity and selectivity discussion. The results of the third catalytic cycle under a wet stream are discussed separately in the end of

catalytic results section to show the effect of water on activity. For alumina-supported catalysts with 2 wt. % Pt loading, 25 mg of a sample was taken. In the case of 1 wt. % zeolite-supported catalysts 50 mg of a sample was used in order to maintain the same weight Pt loading in the reactor. Total gas flow constituted 1050 cm³/min. Sieved fraction of catalysts with grain size 100–200 μm was diluted with silicon carbide (same sieve fraction) to obtain catalyst bed volume corresponding to gas hourly space velocity of 60,000 cm⁻¹. The composition of the gas mixture at the outlet of the reactor was analysed on-line using a Multigas 2030 FTIR spectrometer (MKS Instruments, USA). Conversion of ammonia (X_{NH_3}) was calculated according to $X_{\text{NH}_3} = (1 - C_{\text{NH}_3}^{\text{out}}/C_{\text{NH}_3}^{\text{in}}) \cdot 100\%$, where $C_{\text{NH}_3}^{\text{out}}$ and $C_{\text{NH}_3}^{\text{in}}$ are ammonia concentrations at the reactor outlet and inlet, respectively. Selectivity to products was calculated according to the formula $S_i = n_i \cdot C_i / (C_{\text{NH}_3}^{\text{in}} - C_{\text{NH}_3}^{\text{out}}) \cdot 100\%$, where C_i is product i concentration, and n_i – number of nitrogen atoms in the corresponding product molecule. The nitrogen concentration was calculated from NH₃ conversion and concentrations of other products based on the mass balance.

Kinetic analysis

Reaction orders of ammonia and oxygen were estimated in ammonia oxidation over alumina-supported Pt catalysts. For this purpose, integral reaction rates were measured as functions of concentrations of one of the reactants at constant temperatures. A reaction rate was calculated as an amount of converted ammonia (in mmol) per minute over a gram of Pt under certain conditions. The used catalyst loadings amounted to 25 mg. The same setup and gas flow were employed as for activity and selectivity tests. The data used in the calculations were recorded after the establishment of equilibrium, which took 30–120 min.

Ex situ and operando X-ray absorption spectroscopy

To measure *ex situ* and *operando* X-ray absorption spectra (XAS), the catalysts were loaded in 1.5-mm-diameter quartz capillaries (0.02 mm wall thickness) as 100–200 μm sieved powders with the catalyst bed length of approximately 5 mm. In all cases, spectra at Pt L₃ absorption edge were recorded in transmission mode. For energy shift correction, a platinum foil spectrum was recorded simultaneously.

Ex situ extended X-ray absorption fine structure (EXAFS) spectra

Table 1. Summary of catalyst preparation conditions.

Sample name	Preparation method	Precursor	Preparation conditions
2 wt. % Pt/ γ -Al ₂ O ₃			
PtA-IW			calcined at 400 °C, then reduced in 5 % H ₂ at 400 °C
PtA-IW-500	IWI	Pt(NO ₃) ₂	PtA-IW, additionally calcined at 500 °C in air flow
PtA-IW-700			PtA-IW, additionally calcined at 700 °C in air flow
1 wt. % Pt/ZSM-5			
PtZ-IE	IE	[Pt(NH ₃) ₂]Cl ₂	calcined at 450 °C in air flow
PtZ-IE-R	IE	[Pt(NH ₃) ₂]Cl ₂	as for PtZ-IE, additionally reduced at 400 °C in 5 % H ₂
PtZ-IW	IWI	Pt(NO ₃) ₂	calcined at 500 °C



for the alumina-supported samples were measured at the CAT-ACT beamline at the KIT light source (Karlsruhe, Germany).⁴³ *Ex situ* EXAFS spectra for the zeolite-supported samples were recorded at the P64 beamline of the PETRA III synchrotron radiation source (DESY, Hamburg, Germany). In both cases, the X-ray energy was selected using Si(111) monochromators with a pair of Si mirrors to eliminate higher harmonics. Energy correction and normalisation were conducted in *Athena* software from the *IFEFFIT* package.⁴⁴

Next, the background-subtracted and k^2 -weighted spectra were Fourier-transformed (k -range of 2-10 \AA^{-1} and 2.5-10.5 \AA^{-1} for the alumina and zeolite based samples, respectively). The amplitude reduction factor was received by fitting a Pt foil (structural model from the Inorganic Crystal Structure Database, ICSD, CC 243678). They amounted to $S_0^2 = 0.68$ and $S_0^2 = 0.78$ for the alumina and zeolite supported samples (measured at the KIT light source and PETRA III), respectively. Fitting of EXAFS spectra was conducted in order to refine coordination numbers, interatomic distances, energy shift (δE_0) and mean square deviation of interatomic distances (σ^2). The misfit between the calculated and measured spectra is expressed by ρ . The refining was conducted on k^1 , k^2 , and k^3 -weighted data by a least square method in *Artemis* software from the *IFEFFIT* package.⁴⁴ Structural models for the fitting were based on metallic Pt and PtO₂ structures, ICSD CCs 243678 and 1008935. The zeolite structure model (MFI type) that was used for fitting was described by Meier et al.⁴⁵ Coordinates of cationic positions in the MFI zeolite structure were obtained from Mentzen et al.⁴⁶

Operando quick-scanning extended X-ray absorption fine structure (QEXAFS) spectra were measured at the P64 beamline of the PETRA III synchrotron radiation source (DESY, Hamburg, Germany) using a continuously oscillating Si(111) channel-cut monochromator and the Si mirrors described above. Scanning speed (up and down energy scans) constituted 1 Hz. Energy correction and normalisation for Pt foil reference were conducted in *Athena* software from the *IFEFFIT* package.⁴⁴ Energy correction and normalisation for the spectra of the samples were conducted in *ProQEXAFS* software, v. 2.42.⁴⁷ The spectral components of the recorded QEXAFS spectra were extracted using multivariate curve resolution (MCR) as implemented in the *SIMPLISMA* algorithm built in the *ProQEXAFS* software.⁴⁷ Later on, these components were used to conduct linear combination analysis (LCA) of the spectra in the same program.

The *in situ* setup is similar to the previously described in ref. [48]. Gas composition during the *operando* XAS experiments on Al₂O₃-supported samples was 500 ppm NH₃, 10 vol. % O₂ balanced with He and N₂ mixture. Gas flow constituted 75 cm³/min. Gas composition for the ZSM-5-supported samples was 890 ppm NH₃, 10 vol. % O₂ balanced with He and N₂ mixture. This mixture was fed with the flow rate of 70 cm³/min. For both series of samples, the temperature was increased from 50°C to 400°C with a heating rate of 5 °C/min. Before the *operando* measurements, an additional heating and cooling cycle in this temperature range with the same heating rate was conducted to pre-treat the samples. For calculation of ammonia

conversion and product selectivities, the same approach was used as in the catalytic experiments. A detailed explanation is given on p. S1 of the SI.

In situ DRIFTS

In situ diffuse reflection infrared Fourier transform spectra (DRIFTS) were measured using a VERTEX 70 Fourier transform infrared spectrometer (Bruker) with a Praying Mantis diffuse reflection optics (Harrick) and a mercury cadmium telluride (MCT) detector. 60 mg of catalyst samples with 100-200 μm grain size fraction were measured in the Harrick high temperature cell covered with a flat CaF₂ window.

Gas flow of 200 cm³/min passed downwards through the catalyst bed. Samples were heated in Ar to 300 °C and kept at this temperature for 20 min. Then they were cooled to room temperature and flushed for 20 min. After this, spectra in Ar were recorded and used as background measurements. Then the samples were exposed to 1 % CO in Ar at room temperature for 30 min and subsequently flushed with pure Ar for 30 min. For the PtZ-IE sample, an additional treatment in 0.1 % CO flow (balanced with Ar) for 30 min was conducted at room temperature between the treatment with 1 % CO and pure Ar flushing. DRIFTS spectra were recorded for all samples at the end of each time interval after the gas environment change.

Results and discussion

Sample Characterisation

Ex situ EXAFS. The average particle dispersion was estimated using *ex situ* EXAFS. The results of fitting of EXAFS spectra of the alumina-supported samples are listed in table 2 (the corresponding fits are presented in figs. S1-S3). The best fit for the initial PtA-IW sample includes contribution of only O atoms scattering. The introduction of platinum backscatterers from metallic-like species in the fit model does not improve the fit and results in physically not meaningful coordination numbers (fig. S4, table S1). The use of platinum from PtO₂ in a fit model makes Pt coordination number more realistic. However, it has high uncertainty which exceeds the value of the coordination number itself (fig. S4, table S1). This result, together with the reasonable fitting result for the model including only O atoms in Pt surrounding, indicates an amorphous oxidised state of platinum with a substantial contribution of species with a dispersion close to atomic. Note that the detailed analysis of different fractions of Pt species that can be present in this sample needs to be conducted with complementary techniques, since EXAFS allows to estimate just an average state of a bulk sample. For PtA-IW-500, the fit model already includes a contribution of the second Pt-Pt shell typical for metallic platinum. The average Pt coordination number for this sample corresponds to 0.5-1 nm clusters.⁴⁹ Finally, the Pt-Pt coordination number for PtA-IW-700 was close to 12 indicating high bulk contribution of metallic Pt and thus large nanoparticles with size ≥ 5 nm. In summary, *ex situ* EXAFS analysis reveals that the average particle dispersion decreases with higher calcination temperature. Pt particles are highly dispersed with significant contribution of close to atomic species for PtA-IW,



Table 2. The fitting results of *ex situ* EXAFS spectra at the Pt L₃-edge. The data fits and further information on the fitting parameters are given in fig. S1-S3, S5-S7. [View Article Online](#)
DOI: 10.1039/D2CY02095E

PtZ-IW fits	Scattering atoms	R (Å)	CN	σ^2 (10 ⁻³ Å ²)	δE_0 (eV)	ρ (%)
2 wt. % Pt/ γ -Al ₂ O ₃						
PtA-IW	Pt-O	2.03 ± 0.11	3.1 ± 0.6	5.7 ± 4.4	14.1 ± 2.2	3.4
PtA-IW-500	Pt-Pt	2.76 ± 0.03	4.3 ± 1.7	1.5 ± 4.8	9.0 ± 2.5	2.7
	Pt-O	1.99 ± 0.07	2.8 ± 0.5	0.1 ± 4.3		
PtA-IW-700	Pt-Pt	2.75 ± 0.04	11.5 ± 2.2	4.7 ± 1.9	11.5 ± 2.2	0.7
	Pt-O	1.95 ± 0.03	0.5 ± 0.3			
1 wt. % Pt/ZSM-5						
PtZ-IW	Pt-Pt	2.75 ± 0.04	0.9 ± 0.7	2.2 ± 2.1	9.1 ± 1.6	2.0
	Pt-O	1.99 ± 0.01	3.7 ± 0.6			
PtZ-IE	Pt-Si	2.73 ± 0.05	1.1 ± 0.7	3.1 ± 2.6	12.7 ± 1.8	2.3
	Pt-O	2.02 ± 0.02	4.4 ± 0.8			
PtZ-IE-R	Pt-Si	2.77 ± 0.07	0.4 ± 0.4	0.8 ± 2.5	9.5 ± 2.5	9.7
	Pt-O	1.99 ± 0.02	1.6 ± 0.4			

with small nanoparticles for PtA-IW-500 and big nanoparticles over 5 nm for PtA-IW-700.

The results of EXAFS spectra fitting of the zeolite-supported samples are presented in table 2, and the fits – in figs. S5-S7. Spectra of the incipient-wetness-obtained PtZ-IW sample most reliably show platinum in the second coordination sphere (table 2, fig. S5). Its average coordination number of 0.9 corresponds to very small clusters.⁴⁹

The other two samples, which were synthesised using ion exchange, exhibit the most credible fitting results for the models including O and Si from zeolite as backscatters.

On the contrary, the fits including O and Pt from Pt⁰ result in unrealistic negative coordination numbers of Pt. A fitting attempt with the model including Pt atoms from PtO₂, instead of metallic Pt, yields a similar result for PtZ-IE-R. For PtZ-IE, the coordination number of Pt from the oxide structure is positive but has too high uncertainty. Additionally, this fitting model shows a somewhat higher misfit compared to the model including O and Si as backscatters. Thus, the spectra of the ion-exchanged samples correspond to highly amorphous state which lacks pronounced scattering from defined Pt-Pt distances. A pronounced fraction of the spectra originates from Pt-O and Pt-Si contributions, typical for atomically dispersed Pt. However, the highly amorphous nature does not exclude other dispersed oxidised Pt fractions with low structural order.

Nevertheless, X-ray absorption spectroscopy is a bulk technique that gives an overview over the averaged state of a sample. If a sample is not uniform, for example several fractions of different-sized particles exist, this averaged picture may not be a true representation of any of them. To evaluate the presence of different size fractions and their contributions, EXAFS analysis was complemented with TEM and *in situ* DRIFTS with chemisorbed CO.

TEM. For the more precise particle size determination HAADF-STEM images of the synthesised samples were obtained (fig. 1).

According to their analysis, PtA-IW and PtA-IW-500 consist mainly of two similar fractions of particles with different ratios in their content. The larger fraction contains small nanoparticles of average diameter of 1.7 nm for PtA-IW and 1.8 nm in the case of PtA-IW-500. The lower fraction is represented by dispersed Pt clusters of one to several atoms. Some atomic Pt sites are shown in more detail in magnified images in fig. S11. It is hard to determine the average size of the lower fraction species due to unsharp borders of many of them. It is also clear that for PtA-IW the fraction of clusters is larger than for PtA-IW-500 where small nanoparticles are more frequent. Additionally, on lower magnification images of PtA-IW-500, larger particles of ~10 nm diameter start to become visible (fig. S11). The relative content of these fractions is further estimated with *in situ* DRIFTS of chemisorbed CO.

The PtA-IW-700 sample significantly differs from the other two. While some clusters and individual small nanoparticles are observed (see fig. S11), the main contribution is made by large polydisperse Pt nanoparticles with an average diameter of 13.6 nm.

As for the impregnated zeolite samples, the ones obtained with ion exchange show the most dispersed Pt species. PtZ-IE contains a great abundance of Pt clusters, maybe even single sites and only a minor fraction of small nanoparticles (> 1.2 nm). Some atomically distributed Pt sites in this sample are shown in more detail in a magnified image in fig. S11. The reduced catalyst PtZ-IE-R displays fewer clusters and hardly any individual single sites than the PtZ-IE. Instead, numerous nanoparticles with average diameter of 1.4 nm are present in the TEM images.

PtZ-IW, obtained with incipient wetness impregnation, contains the biggest Pt nanoparticles in the zeolite-supported series with the average diameter of 2.2 nm. The distribution of the nanoparticles on zeolite crystals is not homogeneous. Apparently, this is due the fact that the size of the Pt nanoparti-



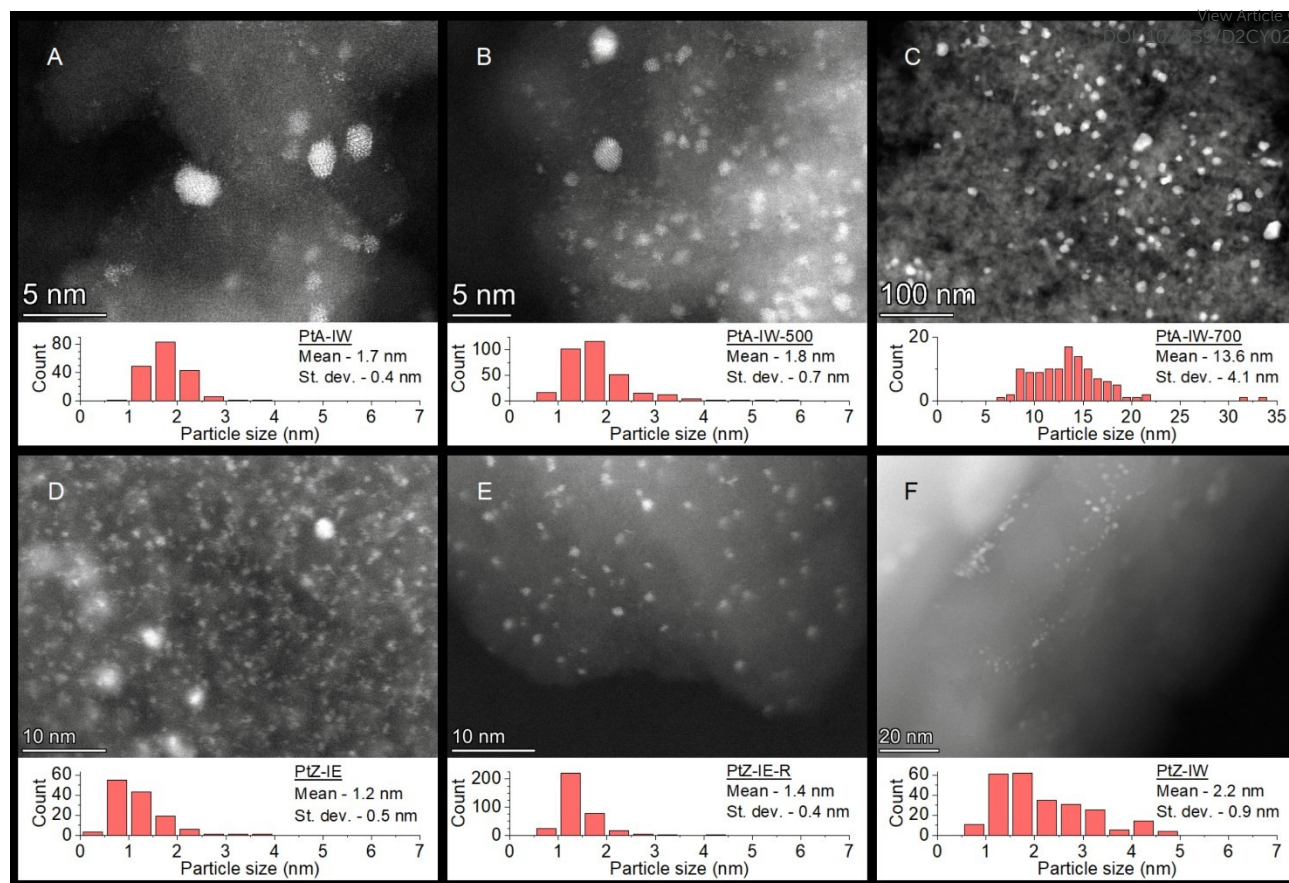


Figure 1. HAADF-STEM images of the synthesized catalysts. Alumina-supported samples: A – PtA-IW, B – PtA-IW-500, C – PtA-IW-700. ZSM-5-supported samples: D – PtZ-IE, E – PtZ-IE-R, F – PtZ-IW. The insets in each image display size distributions of measurable particles for the respective samples.

cles exceeds the zeolite pore and channel diameter. Hence, they can only be located on the outer surface of the zeolite crystals.

In general, Pt species in the zeolite-supported samples are more disperse than the alumina-supported ones and contain almost no large nanoparticles on the bigger-scale TEM images (fig. S11).

For the samples studied, due to big size of support crystals and their low conductivity, part of the single atoms was not distinctly visible in the TEM images. For this reason, to complement the understanding of Pt dispersion and to evaluate contributions of different size fractions, *in situ* DRIFTS spectra of chemisorbed CO were measured for the synthesized catalysts.

***In situ* DRIFTS of adsorbed CO.** Figs. 2 and 3 display *in situ* DRIFTS spectra in CO atmosphere for the zeolite-supported and alumina-supported catalysts respectively. The spectra demonstrate a variety of absorption bands in the range ~ 2200 – 1700 cm^{-1} , typical for carbon monoxide adsorbed on various platinum sites. The bands in the range 1940 – 1745 cm^{-1} correspond to bridged CO.^{50–54} These bands are present in the spectra of all samples and point to presence of Pt clusters and / or particles. Their position does not vary substantially between the samples within the series on one support and their intensity is approximately proportional to the catalyst surface area as will be shown below. Therefore, besides indicating the presence of

some particles in every sample, they are not very informative for Pt particle size estimation. The band around 1660 cm^{-1} in the spectra of alumina-supported catalysts is attributed to carbon dioxide or carbonate species and is typical for alumina support.^{53, 55}

On the contrary, the bands corresponding to linearly bonded CO at wavenumbers above 2000 cm^{-1} are very distinct. The range ~ 2090 – 2000 cm^{-1} contains bands of linearly adsorbed CO on Pt terraces in reduced nanoparticles or clusters^{50, 52, 56–60} (bands highlighted in pink in figs. 2, 3). The shift to higher wavenumbers indicates decrease of platinum particle size⁵⁶ down to single sites including cationic ones that were reported to show their absorption band starting from 2090 cm^{-1} ^{56, 59, 61, 62} and above. The area of ~ 2120 – 2090 cm^{-1} (highlighted in yellow in fig. 2, fig. 3) is the one in which the bands of platinum single sites are most frequently reported.^{56–63} According to literature, the band at 2090 cm^{-1} corresponds to CO adsorbed on more reduced platinum that can be either partially reduced single sites^{60, 61} or corner and edge metal atoms which are abundant on small nanoparticles.^{57, 60, 64} In other works^{57–59, 63}, CO on Pt single sites shows absorption bands around 2120 – 2100 cm^{-1} . This range is also typical for platinum in ionic (oxidised) state that forms monocarbonyl complex and are not necessarily single sites.^{51, 58, 60, 61} Except for the difference in oxidation state, a reason for the difference in the



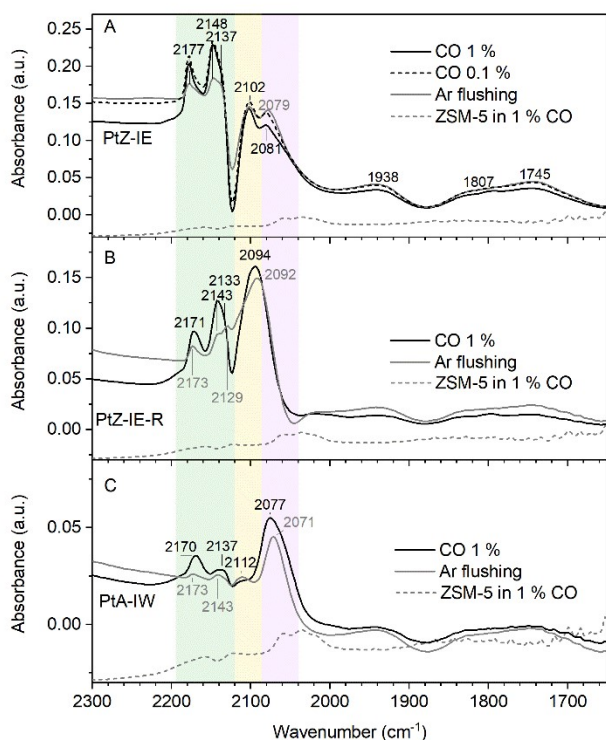


Figure 2. DRIFTS spectra of CO adsorbed on ZSM-5-supported catalysts: A – PtZ-IE sample; B – PtZ-IE-R sample; C – PtZ-IW sample. Black line – spectra in 1 % CO flow. Dashed black line – spectrum in 0.1 % CO flow. Grey line – spectra recorded during Ar flushing after switching off CO flow. Dashed grey line – spectrum of ZSM-5 support in 1 % CO flow.

reported Pt single site absorption frequencies can also be location in a different position of a zeolite network.⁵⁶ Finally, the bands above ~ 2120 cm^{-1} , highlighted in green in fig. 2, belong to polycarbonyl complexes of ionic Pt.^{51, 57, 60} They are found only on the zeolite-supported samples and are absent on the alumina-supported ones. The spectra of pure ZSM-5 support in CO exhibit absorption bands of gaseous carbon monoxide at 2160 and 2125 cm^{-1} – in the same range as the polycarbonyls (fig. 2, grey dashed line). However, these bands have low intensity compared to the main bands of the zeolite-supported spectra.

Therefore, their interference with determining types of Pt sites is minor. The low intensity bands at 2170 and 2125 cm^{-1} on alumina-supported samples in fig. 3 belong to gaseous CO and quickly disappear during Ar flushing.⁶⁰ As it is apparent from the literature data above, only absorption frequency may be not sufficient to unequivocally distinguish between small nanoparticles/clusters, oxidised platinum particles and single sites. The exception are probably the polycarbonyls on isolated Pt^{n+} ions ($n=1-3$), which exhibit their absorption bands above 2120 cm^{-1} .^{51, 60} For other species, a way to discriminate them from single sites is to vary the coverage of CO and follow the frequencies of the observed absorption bands. For isolated platinum atoms, the band position is supposed to be stable due to absence of dipole-dipole interaction of adsorbate molecules. This approach has been demonstrated for absorption bands in

the 2120-2090 cm^{-1} range⁵⁶⁻⁵⁹ (yellow in fig. 2). To change the CO surface concentration in this study, we switched off CO flow after keeping the samples in its atmosphere so that pure Ar flushing remained. For strongly absorbed CO, certain conditions (e.g. high vacuum) may be required to change its surface coverage. Hence, even a stable band position in this region requires careful consideration before it can be assigned to atomically dispersed Pt. However, if a band changes its energy and symmetry, like it will be shown further, it allows to exclude its origin from single site species.

The PtZ-IE sample possesses the most intense CO-bands of all zeolite-supported catalysts. This can be an indirect evidence of the highest Pt dispersion. The sample exhibits pronounced bands for polycarbonyls and monocarbonyl on ionic Pt (~ 2177 -2100 cm^{-1} , areas highlighted in green and yellow respectively). A closer look at polycarbonyl bands around 2177 and 2137 cm^{-1} reveals their possible origin from platinum coordinating not only to CO, but also to Cl, probably remaining from the precursor.^{65, 66} All the carbonyl bands retain their position during flushing with Ar, which is an indication of highly dispersed platinum. These absorption frequencies correspond to polycarbonyls on isolated platinum in ionic state.^{51, 60} The less intense band at around 2080 cm^{-1} suggests a concurrent presence of some small nanoparticles. Light red shift by 2 cm^{-1} implies minor dipole-dipole interactions not found for single sites. The low intensity bridged CO bands in the 1940-1745 cm^{-1} region reveal possible presence of few bigger Pt particles with small surface area.

PtZ-IE-R catalyst, which underwent additional reductive treatment after ion exchange, exhibits a similar profile in the polycarbonyl area, but differs in the monocarbonyl and reduced platinum wavenumber ranges below ~ 2120 cm^{-1} (yellow and pink highlights in fig. 2B). The most intense absorption band is now at 2094 cm^{-1} corresponding to reduced single sites or small clusters. Slight red shift by 2 cm^{-1} may indicate rather the latter type of Pt species. As for the polycarbonyl bands, they also start to exhibit a minor energy shift by 2-3 cm^{-1} , which implies possible clustering of oxidised Pt atoms. The lower overall intensity of absorption bands signifies lower total dispersion compared to the unreduced PtZ-IE sample.

The trend of decreasing absorption band intensities and, hence, lower platinum dispersion further continues for the incipient-wetness-impregnation-obtained PtZ-IW catalyst. The absorption band corresponding to reduced Pt species (pink-highlighted range in fig. 2C) is at lower energy of 2077 cm^{-1} typical for small Pt nanoparticles. A higher red shift of 6 cm^{-1} during Ar flushing also evidences larger particle size compared to the PtZ-IE catalysts. The profile of carbonyl bands on ionic Pt, which are visible above ~ 2090 cm^{-1} (ranges of green and yellow colours in fig. 2C), is also slightly different for this sample. It has a new band at 2112 cm^{-1} that may correspond to Pt^{2+} monocarbonyl species or, together with the other two bands at 2170 and 2137 cm^{-1} , signify tricarbonyl Pt^+ species.⁵¹

Unlike the zeolite-supported samples, the alumina-based catalysts exhibit absorption bands which correspond mainly to metallic platinum nanoparticles and clusters without bands of



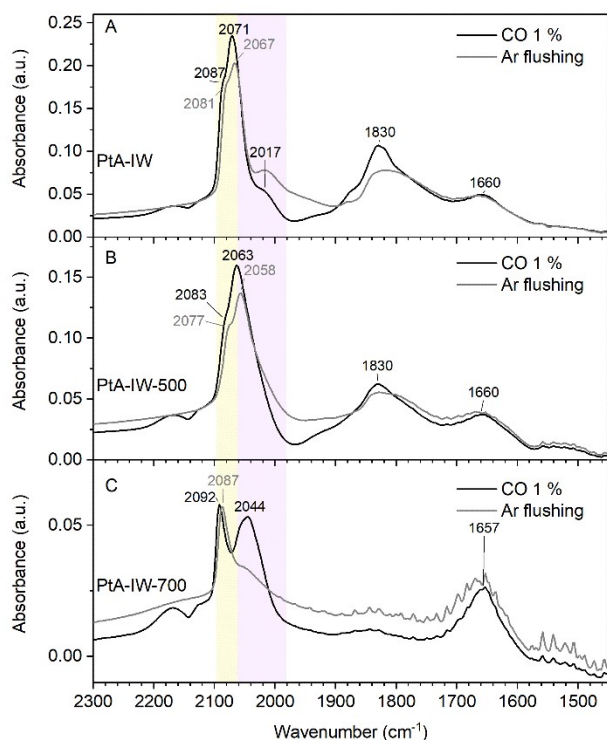


Figure 3. DRIFTS spectra of CO adsorbed on alumina-supported catalysts: A – PtA-IW sample; B – PtA-IW-500 sample; C – PtA-IW-700 sample. Black line – spectra in 1 % CO flow. Grey line – spectra during Ar flushing after switching off CO flow.

polycarbonyls. Thus, only two zones containing information about Pt dispersion can be distinguished for these samples. The first one, around 2090-2080 cm^{-1} (yellow in fig. 3), corresponds to platinum clusters or small nanoparticles. Assigning these bands to clusters rather than reduced single sites is based on a relatively significant energy shift of 4-6 cm^{-1} , which is not typical for atomically dispersed platinum. The second energy range from 2090 to 2000 cm^{-1} (pink in fig. 3) contains bands that originate from platinum nanoparticles. The energy of the main band in this region decreases with the increase of the temperature of catalyst treatment. It has the highest value of $\sim 2071 \text{ cm}^{-1}$ for the untreated sample PtA-IW, lower value of $\sim 2060 \text{ cm}^{-1}$ for the sample PtA-IW-500, treated at 500 $^{\circ}\text{C}$, and the lowest with the value 2040 cm^{-1} for the sample Pt-IW-700 treated at 700 $^{\circ}\text{C}$. This decrease of the absorption energy is an indication of particle size increase.⁵⁶ The higher intensity of the absorption bands below 2090 cm^{-1} (pink in fig. 3) for PtA-IW and PtA-IW-500 indicates higher fraction of nanoparticles compared to small clusters. A higher relative intensity of the band at 2092 cm^{-1} does not necessarily mean the inverse ratio for the PtA-700, because the intensity of all bands is in general significantly lower for this sample hinting at lower Pt surface area and bigger particle size. In general, the spectra of the alumina-supported catalysts tentatively reveal the presence of two types of platinum sites, one of which being small Pt clusters and another, dominating one, being nanoparticles. The size of the nanoparticles grows with the increase of temperature of catalyst treatment.

Characterisation summary. A short summary of the results of the characterisation techniques used is shown in Table 3. In general, all samples contain some fraction of single sites, clusters and nanoparticles with different ratios.

For PtA-IW sample, TEM data reveals the presence of two main fractions – platinum single atoms and clusters together with small nanoparticles with a diameter of 1.7 nm. *In situ* DRIFTS demonstrates the predominance of clusters. This is confirmed with *ex situ* EXAFS results showing the average coordination number typical for single atoms and lack of ordered Pt structure. As EXAFS alone usually cannot fully prove single site structure,⁶⁷ its combination with other techniques, like TEM and DRIFTS, is needed.³⁸

Although the fractions of Pt particles in PtA-IW-500 are practically the same as in PtA-IW, the general platinum dispersion is smaller. Because of the additional treatment at 500 $^{\circ}\text{C}$, the average nanoparticle size slightly increases to 1.8 nm. *In situ* DRIFTS results reveal that this also leads to redistribution of Pt atoms between the fractions, and nanoparticles with a diameter of 1.8 nm prevail over clusters and single sites. *Ex situ* EXAFS analysis shows the average coordination number of platinum reaching the values typical for 0.5-1 nm clusters. Together with the appearance of Pt in the coordination environment, it signifies the increase in Pt particle size.

Treatment of PtA-IW at 700 $^{\circ}\text{C}$ leads to a considerable decrease in the number of clusters and single sites and sintering of nanoparticles which increase their average size to 13.6 nm. *In situ* DRIFTS spectra contain absorption bands of low intensity implying the general decrease of dispersion. The absorption bands originate from a small number of single sites or clusters and bigger nanoparticles with small surface area. *Ex situ* EXAFS results are in line with these observations. They exhibit the average coordination number almost as high as in the case of bulk platinum suggesting platinum particle size of $\geq 5 \text{ nm}$. Zeolite-supported catalysts generally show higher dispersion for ion-exchanged samples compared to the incipient-wetness-impregnated one. Thus, TEM images of PtZ-IE reveal high number of small clusters and even single sites together with small nanoparticles of 1.2 nm diameter. The DRIFTS results of this sample demonstrate the prevalence of isolated Pt ions in it. The ion-exchanged sample PtZ-IE-R that underwent reductive treatment contains Pt with lower dispersion. As revealed by TEM, it contains 1.4 nm nanoparticles together with some Pt clusters. According to DRIFTS, it also contains a number of Pt single sites, but the main fraction is Pt in a state of reduced clusters. Finally, the *in situ* DRIFTS spectra of the PtZ-IW sample display low intensity absorption bands signifying its low dispersion. The bands correspond to small oxidised nanoparticles and a low number of Pt clusters. It is in line with the TEM results that reveal mainly nanoparticles of 2.2 nm average diameter. *Ex situ* EXAFS confirms the trend in the increase of Pt particle size for the IW sample compared to the IE-ones. However, it overestimates the sample dispersion compared to *in situ* DRIFTS. This may be caused by lower average particle size for the zeolite-supported samples compared to the alumina-supported ones, higher polydispersity



Table 3. Summary of the characterisation results

View Article Online
DOI: 10.1039/D2CY02095E

Sample	EXAFS	TEM	DRIFTS
2 wt. % Pt/ γ -Al ₂ O ₃			
PtA-IW	high dispersion, disordered structure with significant contribution of atomically distributed Pt	single atoms and clusters; 1.7 nm nanoparticles	clusters are predominant
PtA-IW-500	clusters of 0.5-1 nm size	single atoms and clusters; 1.8 nm nanoparticles	small nanoparticles are predominant
PtA-IW-700	nanoparticles of ≥ 5 nm size	13.6 nm nanoparticles; individual clusters	nanoparticles are predominant
1 wt. % Pt/ZSM-5			
PtZ-IE	high dispersion, disordered structure with significant contribution of atomic Pt	single atoms and clusters; 1.2 nm nanoparticles	single atoms and clusters are predominant
PtZ-IE-R	high dispersion, disordered structure with significant contribution of atomically distributed Pt	clusters, individual single sites; 1.4 nm nanoparticles	clusters are predominant
PtZ-IW	small clusters	2.2 nm nanoparticles	nanoparticles are predominant, a substantial number of small clusters

of the former ones and Pt being in a more amorphous state. In this case, higher number of smaller particles or disordered crystallites lowers the average coordination number and backscattering on neighbouring Pt atoms in Pt coordination environment that are observed in *ex situ* EXAFS.

Catalytic tests

Alumina-supported platinum. To establish structure-activity relationships for the synthesized and characterised samples their activity and selectivity profiles were measured in a laboratory reactor during temperature programmed reaction (cf. experimental, results in fig. 4). In general, the catalytic performance for all three alumina-supported samples followed the same trend. When the light-off starts, selectivity towards N₂ is the highest. After reaching 100 % NH₃ conversion, it decreases. At slightly higher temperature, N₂O starts to prevail. Simultaneously, NO_x yield increased and became predominant at higher temperatures (above ~ 300 °C). Despite these similarities, a clear structure sensitivity is observed since the activity increases with Pt particle size. The PtA-IW-700 sample with large Pt nanoparticles shows 50 % conversion (T_{50%}) at 209 °C. It is followed by the less active PtA-IW-500, which contains predominantly small nanoparticles, with T_{50%} at 224 °C. A more pronounced activity downturn is observed for Pt-IW which has the smallest particles and clusters in the as-prepared catalysts, many of which are composed only of several atoms. T_{50%} for this catalyst increases to 247 °C. The observed activity trends are reproducible also during cooling in the reaction mixture (light-out) with slight hysteresis not exceeding 10 °C (fig. S12).

The variation in platinum size on the nanometre scale does not affect catalyst performance as strongly as the change on the

subnanometre (cluster) scale. A narrow T_{50%} range for Pt nanoparticles of different sizes at high, close to real-application oxygen concentration, was reported earlier.^{30,31} Expanding this range to lower activity zone for smaller particles hints on the important role of particle size additionally to the Pt oxidative behaviour widely described in literature.^{26, 27, 31-33} It was postulated in the previous studies that that specific ensembles of Pt atoms are required for ammonia activation through oxygen-assisted dissociation. The ensembles that are reported to be optimal for this step and to have the lowest energy barriers are step-edge B5-sites, for example Pt(211) facets.^{14, 36, 68-70} According to literature, Pt nanoparticles of less than 5 nm have spherical shape in air with no distinct crystal faces on their surface.⁷¹ At the same time, Pt(211) facets result in the lowest surface energy for small nanoparticles below 5 nm in oxidative media.⁷² It is also reported that these facets have a very low probability to be present on transition metal particles with size below ~ 2 nm.³⁶ The reason for this is a too small number of atoms to form a step site on a small particle retaining an energy-efficient spherical shape.^{36, 73, 74} Thus, the fraction of B5 sites on particles below ~ 2 nm diameter is close to 0 and abruptly increases around 2 nm constituting a maximum surface concentration that further gradually diminishes with particle size increase in favour of terrace sites.^{73, 74} In this study, we observe a sharp increase in ammonia oxidation activity in the size range of ~ 2 nm at which surface B5-sites are reported to emerge. The role of particle size in determining Pt activity appears to be more crucial at realistic NH₃:O₂ ratios and pressures than a commonly reported Pt oxidation state. A number of studies highlight the superior activity of reduced platinum compared to oxidised one in ammonia oxidation reaction.^{26, 27, 30-34} However, it was shown that this factor becomes less important at high oxygen concentrations at atmospheric pressure.³⁰ Although pre-reduced and pre-oxidi-



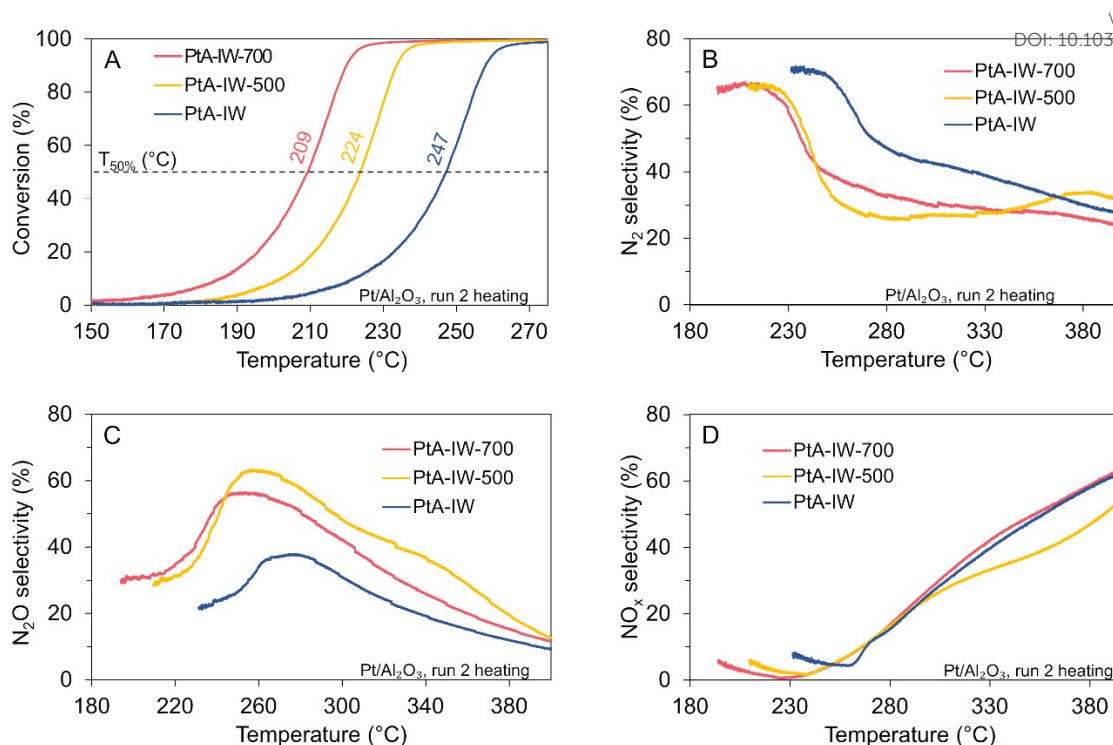


Figure 4. Catalytic tests results for the alumina-supported catalysts during the second light-off in reaction mixture. A – conversion; B – selectivity to N_2 ; C – selectivity to N_2O ; D – selectivity to NO_x . Red line – PtA-IW-700; orange line – PtA-IW-500; blue line – PtA-IW. Reaction feed – 500 ppm NH_3 , 13 % O_2 in N_2 . Flow – 1050 cm^3/min . GHSV = 63,000 cm^{-1} . Loading – 25 mg of 2 wt. % Pt catalyst. Heating rate of 3 $^{\circ}C/min$.

sed catalysts with similar Pt dispersions performed significantly differently at 4 % O_2 concentration, they had almost equal activity in a reaction mixture containing 13 % O_2 already after the first catalytic cycle. This study also evidences the less significant influence of oxidation state on activity and a major role of particle size which may be linked to the oxidation state as the smaller particles / clusters oxidise easier. Comparing *ex-situ* X-ray absorption near-edge structure (XANES) spectra of the catalysts tested (fig. S13), one can see that PtA-IW-500 is more active than PtA-IW despite the first one is more oxidised and prepared from the latter one. The sign of a more reduced state of PtA-IW is a lower absorption intensity of its XANES spectrum near the adsorption edge, which is also called white line, compared to the white line for PtA-IW-500. In general, the PtA-IW spectrum is also closer to the Pt foil reference than the one of PtA-IW-500. Evidently, bigger particle size of the latter catalyst is playing a more important role in its activity than the oxidation state. It is also interesting to compare the performance of PtA-IW, after reductive treatment, with the same catalyst before reduction (fig. S14). The catalytic performance of this sample before and after reductive treatment is almost identical despite a great difference in oxidation state and the unreduced sample almost reaching the spectrum of PtO_2 in its white line intensity (fig. S13). Since the difference of Pt oxidation state in PtA-IW before and after reduction is drastic (significantly higher than the change of oxidation state under reaction conditions, cf. later), its almost unchanged performance points out that it is the particle size that is at the origin of the structure sensitivity. Note that this

may still also be coupled to the oxidation state if the catalyst structure changes under reaction conditions. Nevertheless, favourable ensembles of surface Pt atoms seem to be present for large particles.

Regarding selectivity to nitrogen, its trend appears to be inverse to activity – PtA-IW with the smallest particle size is the most selective to N_2 in the series. PtA-IW-500 and PtA-IW-700 are less selective, but no clear trend can be seen between the two of them. They demonstrate similar relatively high N_2 selectivity at low temperatures. In the intermediate temperature range, PtA-IW-500 shows the lowest N_2 selectivity and is the most selective to N_2O of all three catalysts. At high temperature, especially during light-out (fig. S12), PtA-IW-500 exceeds PtA-IW-700 in its selectivity to nitrogen. For all three samples, NO_x selectivity rises monotonously starting from ~ 240 $^{\circ}C$ and is the lowest for PtA-IW-500 mainly in favour of N_2O . Higher selectivity for less active catalysts was already described in literature.³⁰ T. Hansen reported³¹ the opposite trend but notably only for low temperatures. Literature studies suggest different Pt surface coverage of N_{ads} , O_{ads} or NO_{ads} as the reason for different product yields in this system.⁷⁵⁻⁷⁸ The observation that selectivity to N_2 decreases as soon as conversion reaches 100 % in this and other works^{30, 32} complies with this explanation. In these conditions, the catalysts with bigger particles on which ammonia is oxidised faster yield surfaces poorer in ammonia-derived species, which decreases selectivity to nitrogen.

Zeolite-supported platinum. The general particle size-activity correlation for the zeolite-supported samples is analogous to



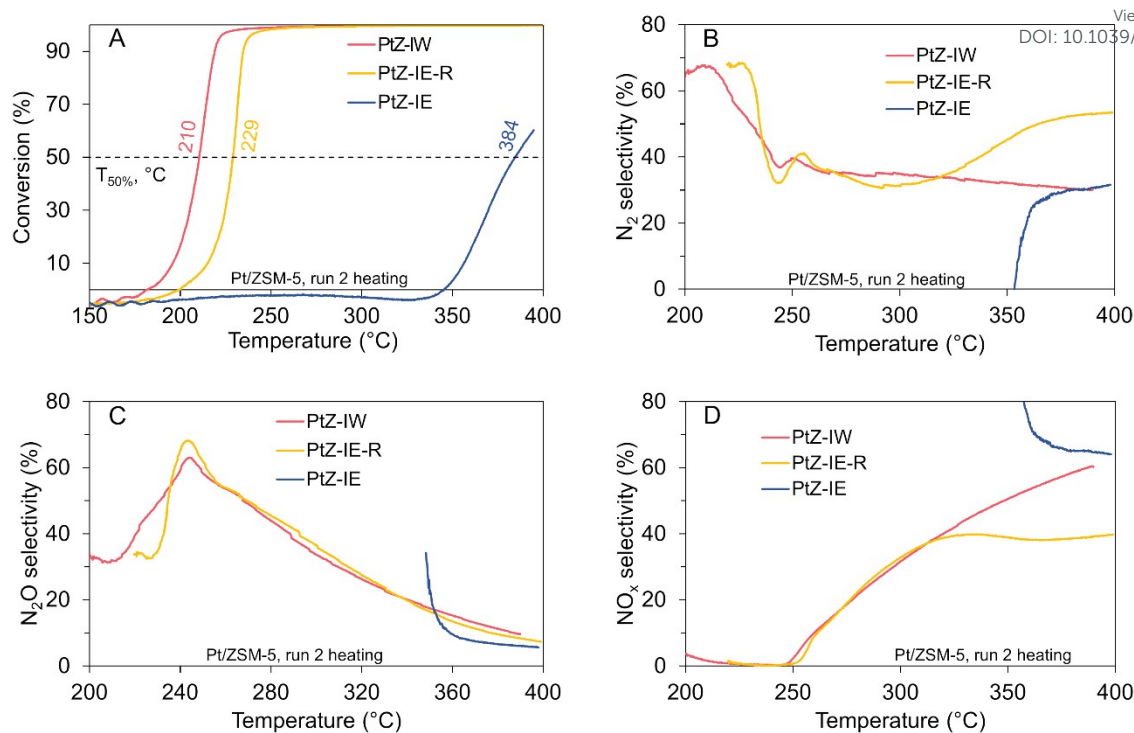


Figure 5. Catalytic test results for the ZSM-5-supported catalysts during the second light-off in reaction mixture. A – conversion; B – selectivity to N_2 ; C – selectivity to N_2O ; D – selectivity to NO_x . Red line – PtZ-IW; orange line – PtZ-IE-R; blue line – PtZ-IE. Reaction feed – 500 ppm NH_3 , 13 % O_2 in N_2 . Flow – 1050 cm^3/min . GHSV = 63,000 cm^{-1} . Loading – 25 mg of 2 wt. % Pt catalyst. Heating rate of 3 $^{\circ}C/min$.

the trend observed for the alumina-supported samples. The conversion rises with Pt particle size from rather inactive PtZ-IE with high amount of atomically dispersed Pt to PtZ-IW with the highest fraction of nanoparticles in the series (fig. 5). Apparent negative conversion at low temperatures originates from desorption of stored NH_3 from zeolite with temperature rise.

$T_{50\%}$ values for the nanoparticle-dominated sample PtZ-IW (210 $^{\circ}C$) and cluster-dominated sample PtZ-IE-R (229 $^{\circ}C$) resemble those of the corresponding alumina-supported samples with particle sizes in a similar range – PtA-IW-700 and PtA-IW-500. Remarkably, the sample PtZ-IW with 2.2 nm nanoparticles has practically the same $T_{50\%}$ as PtA-IW-700 with much bigger average particle diameter of 13.6 nm. At the same time, the sample PtA-IW-500 with predominant nanoparticles of 1.8 nm is less active.

Activity of the PtZ-IE sample with predominantly Pt single sites / small clusters is drastically poorer. Its $T_{50\%}$ during light-off constitutes 384 $^{\circ}C$ which is significantly higher than the range of light-off temperatures reported in literature for similar reaction conditions.^{30, 31} PtZ-IE also stands out in its hysteresis. While for PtZ-IW and PtZ-IE-R hysteresis is slightly larger than for the alumina-supported samples with Pt particles in similar size range (PtA-IW-700 and PtA-IW-500 respectively), for PtZ-IE it is as big as 143 $^{\circ}C$ (cf. fig. 5 and fig. S16). This cannot be explained only with the change of the structure of the sample under the reaction conditions. Different activity in the first and the second catalytic cycle shown in fig. S17 indicates that some structural changes do occur. However, the effect from them is smaller than the observed hysteresis in both cycles. Such a distinct

behaviour of the PtZ-IE sample together with its low activity is a strong hint for a different reaction mechanism. Selectivity to N_2 for all three zeolite-supported samples increases during the light-out with decreasing particle size (fig. S15). This trend, with the exception of the single-site-dominated sample (PtZ-IE), is also observed during the light-off. Samples PtZ-IE-R and PtZ-IW show similar selectivity to N_2 at low temperatures, i.e. below ~ 315 $^{\circ}C$ during the light-off and ~ 280 $^{\circ}C$ during light-out. At higher temperatures selectivity to nitrogen increases from ~ 40 % to 50 % in the case of PtZ-IE-R and decreases from the same initial level to 30 % in the case of PtZ-IW. In the case of the single-site-dominated sample PtZ-IE, selectivity to nitrogen is the highest among all zeolite-supported samples during cooling. It decreases from ~ 80 % at 200 $^{\circ}C$ to ~ 50 % at 400 $^{\circ}C$. During the light-off this sample shows a completely different behaviour producing almost exclusively NO_x (mostly NO) at low conversions. With conversions above 10 % the selectivity of this sample becomes similar to that of the PtZ-IW with ~ 60 % NO_x and ~ 30 % N_2 yields. In general, selectivity to nitrogen is higher for zeolite-supported samples than for alumina-supported samples. This can be explained with the higher acidity and ability to store more ammonia in zeolites which ensures higher coverage of surface N-intermediates and improves N_2 yield.^{79, 80}

The peculiar performance of the sample containing Pt single sites and small clusters may be explained with unavailable Pt ensembles for the mechanism of the Ostwald process as the activation step of O-assisted ammonia dissociation on single sites / small clusters is hardly possible. An additional factor contributing to the low activity of single sites / small clusters



may be their coordination to =O or -OH-groups of the zeolite which limits adsorption of the reactants. As in the case of the alumina-supported catalysts, the oxidation state of this sample does not seem to be an essential factor for its activity. According to the *ex situ* XANES spectrum of PtZ-IE (fig. S19) this catalyst is oxidised with an intermediate oxidation state between Pt(0) and Pt(IV). This can be deduced from the white line height almost in the middle between the white lines of the two references. In contrast, a more active PtZ-IE-R catalyst spectrum has a less intense maximum, which points to its more reduced state. Nevertheless, the lowest activity of PtZ-IE cannot be explained with Pt being more oxidised, because the most active sample in the series, PtZ-IW, is even more oxidised than the least active PtZ-IE. Hence, also for the zeolite-supported catalysts, the explanation of activity difference should be mainly based on the particle size which enables or prevents existence of B5 Pt sites for efficient ammonia activation.

Given the constraints for the Ostwald mechanism at critically small Pt single sites and clusters, a more likely option remains the selective catalytic reduction (SCR) of NO_x with NH₃ that under these conditions also occurs on Pt.⁸¹ In this case, NO_x can be produced on less abundant Pt nanoparticles or clusters that are also present in PtZ-IW, according to DRIFTS. Higher selectivity to N₂ at high temperatures during cooling supports the SCR mechanism hypothesis. Significantly lower light-off activity and lower selectivity may result from inhibition of the SCR mechanism while the catalyst is saturated with some of adsorbates that are not on the catalyst surface during cooling down. A common adsorbate that poisons the SCR Cu and Fe catalysts is ammonia which prevents re-oxidation of active sites.⁸² Another adsorbate that is abundant on the surface during catalyst heating and absent during cooling is water. Its presence in the case of SCR on Cu was shown to keep catalyst in the oxidised state and its desorption – to dynamically alter catalyst activity.^{83, 84}

Dependence of reaction orders on particle size. To gain a better understanding of different activity regimes observed for catalysts with different particle sizes, reaction orders by oxygen and ammonia were estimated. For this purpose, integral reaction rates were measured for the alumina-supported samples in reaction feeds with varying concentrations of either oxygen or ammonia (figs. S20-S21). The increase of oxygen concentration led to decline in the reaction rates for all samples (see fig. S20). This implied negative reaction orders and deactivation of catalysts by oxygen regardless of particle size. Evaluations of the factors behind the negative reaction order is beyond the scope of this paper. On the contrary, the reaction rate increased with rising ammonia concentrations (fig. S21). However, the extent of this rate growth varied. This was expressed in different reaction orders by ammonia for catalysts with altering particle sizes which are visualised in fig. S22. More specifically, the reaction orders at 200 °C for PtA-IW-500 and PtA-IW-700, the samples with particle sizes in nanometre range, were about 0.3 and 0.5 respectively. With temperature increase to 225 °C the reaction orders almost doubled – to about 0.6 and 1 accordingly. It is important to note that for PtA-IW-700 the apparent reaction order at 225 °C may be compromised since

the catalyst was approaching full conversion. Nevertheless, the trend towards the increase would be still kept for this catalyst. On the other hand, the trend of the reaction order for the sample with predominantly sub-nanometre Pt clusters was different. The apparent reaction order at 200 °C could not be identified due to lack of observable activity. In turn, at 225 °C the reaction order was 0.25. Notably, with temperature increase to 235 °C, it remained almost constant and amounted to 0.22. These comparably low values of the reaction order which are stable within the tested temperature range point to a possibly different mechanism of ammonia activation on sub-nanometre Pt particles compared to particles of 2 nm diameter and larger.

General activity and selectivity trends. To compare the trends in activity not only based on conversion but also in terms of reaction rate, turnover frequencies (TOFs) of ammonia oxidation on different samples are reported in fig. S23 (see also later discussion).

The normalised reaction rates per surface atom of Pt allow for a better comparison of the catalytic activity of Pt on different supports. For this purpose, TOFs of catalysts on alumina and zeolite with similar particle sizes are presented in fig. S25. Among the catalysts with a particle size of about 2 nm (1.8 nm for PtA-IW-500 and 2.2 nm for PtZ-IW) the zeolite-supported one was about 1.4 times more active. This can be explained with higher acidic properties of ZSM-5 compared to alumina. Such behaviour is in line with the studies of Wang et al.⁸⁵ who highlight increased activity of ASCs containing acid sites. They reported that rate of ammonia oxidation positively correlated with the number of acid sites for catalysts containing Pt with particles in nanometre size range. Nonetheless, in this study, the samples with Pt dispersed in a sub-nanometre range showed the opposite activity trend. Specifically, among the samples containing high number of Pt clusters, the alumina-supported one was 1.4 times more active (PtA-IW and PtZ-IE-R in fig. S25). This might be another indication of a different mechanism of ammonia activation on sub-nanometre Pt particles. However, this observation needs to be treated with caution and in the context of other results, since the particles in PtA-IW and PtZ-IE-R are not monodisperse with some larger particles.

In spite of the evident influence of the catalyst support on activity, the effect of particle size turns out prevailing and determining the overall catalyst activity. While the support variation changed TOF by about 1.4, the particle size increase from single sites to clusters and from clusters to nanoparticles changed the reaction rate by orders of magnitude (see fig. S23). Therefore, all the studied catalysts on the two supports form the same activity trend in the TOF dependence on particle diameter. It appears that after reaching a certain size around 2 nm, the activity of ammonia oxidation, normalised by Pt surface, starts to depend on Pt particle size relatively modestly. Before this threshold, the rate dependence on particle size is exponential, while after it still increases but with a linear trend. As discussed above, Pt B5 sites, which were shown to facilitate O-assisted ammonia dissociation, can appear on Pt particles starting from this size.



To analyse the impact of the support on selectivity, alumina- and zeolite-based samples with similar light-off profiles were compared in fig. S26. Zeolite-supported catalysts demonstrated higher N_2 yield at elevated temperatures when ammonia conversion was full. This was true for both heating and cooling in reaction mixture. Zeolite-supported catalysts were still generally more selective at low temperatures and under incomplete ammonia conversions during cooling. However, during heating in reaction mixture alumina-supported samples generally produced more N_2 . As shown in literature by Wang et al.⁸⁵ and Lin et al.⁸⁶, the overall higher selectivity of the zeolite-supported samples is explained with the higher acidity of the support and, particularly, with higher number of Brønsted acid sites. The latter are much more abundant on the zeolite than on the alumina and, together with Lewis acid sites, act to form the ammonia pool on the surface of the support enabling constant supply of ammonia to active Pt species.

Effect of water on activity. TOF was calculated also for the reaction mixture containing water and carbon dioxide (fig. S27). CO_2 was shown to have a minor effect on activity of Pt.³⁰ However, water deactivated the catalysts decreasing TOF by about 6-24 times (fig. S29). Since, oxygen was found to poison Pt in kinetic experiments, the deactivation by water could take place due to the increased oxidative potential of the reaction mixture. An additional factor, might be competition for adsorption sites between water and ammonia. The extent of the deactivation by water varied depending on particle size and

support (fig. S29). Catalysts with smaller particles, were less affected by water than catalysts with larger particles. Probably, this was due to the fact that the smaller particles were already stronger poisoned by oxygen. Zeolite-supported catalysts showed higher TOF drop in wet stream than alumina-supported catalysts with comparable Pt sizes (fig. S29). Probably, this happened because of competition between water and ammonia for adsorption on Lewis acid sites, thus, decreasing amount of NH_3 stored in the vicinity of active sites.

Nevertheless, the general trend of rate dependence on particle size was still the same as in the dry feed with an inflection point at about 2 nm (fig. S27). This shows that the reaction mechanism does not change in presence of water. Therefore, further XAS experiments were conducted in dry feed.

Operando QEXAFS studies

Alumina-supported platinum. In order to study the structure and dynamics of Pt sites during ammonia oxidation, *operando* QEXAFS spectra of the catalysts described above were recorded. To visualise changes in Pt white line region during the light-off in the reaction mixture, the corresponding XANES region of the QEXAFS spectra are presented as contour plots with energy on x-axis, temperature on y-axis and colour-coded normalized absorbance.

The contour plot for the PtA-IW-500 is shown in fig. 6C. This

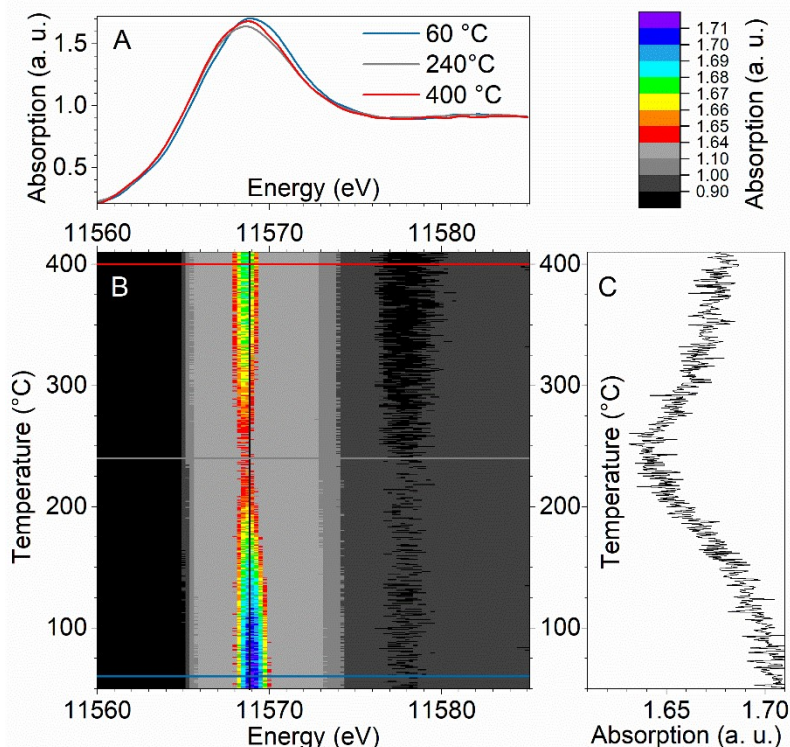


Figure 6. Contour plot of PtA-IW-500 *operando* Pt L_3 -edge XANES spectra measured during the light-off in reaction mixture (500 ppm NH_3 and 10 % O_2 in inert). A – spectra with three most distinct white line shapes (energy profiles from the contour plot). B – the contour plot. C – absorption profile at the energy close to maximum absorption (11568.9 eV). Reaction feed – 890 ppm NH_3 , 10 % O_2 in inert. Flow – 75 cm^3/min (corresponds to a GHSV of about 127,000 h^{-1}). Loading – 50 mg of 1 wt. % catalyst. Heating rate – 5 $^{\circ}C/min$. 2 wt. % Pt catalyst of 100-200 μm sieved fraction was loaded into a 1.5-mm-diameter quartz capillary to form a bed length of ~ 5 mm.



plot can be imagined as a “top view” of a series of XANES spectra measured at different temperatures. The bottom right graph in the fig. 6 represents a temperature profile of normalized absorption of the spectra around their maxima (11568.9eV). The top left graph in the figure shows selected XANES spectra at constant temperatures at which the white line shapes differ most. It is evident from the plot that for PtA-IW-500, all most distinct white line shapes corresponded to partially oxidized Pt. Their intensity is between Pt foil and to PtO₂ references (fig. S30A).

The slight but distinct changes in the Pt white line of these spectral components indicate that the main changes in Pt state occur on its surface with to a great extent unchanged core. Initially, the white line intensity decreases during heating in the reaction mixture and reaches its minimum around 240 °C. Then it becomes more intense again with further heating. Following the white line maximum along the temperature one can see that it shifts to lower energies by ~0.5 eV. These tendencies in white line intensity indicate reduction in the reaction mixture with the highest reduction extent at ~240 °C and then re-oxidation at even higher temperatures.^{87, 88} The absorption maximum shift to lower energies indicates that the oxidised states at high and low temperatures have different coordination environments and, thus, are not equal.^{87, 89}

Catalytic data for the sample PtA-IW-500 recorded during *operando* QEXAFS measurements is shown in fig. 7A. The trends are the same as in laboratory tests. Rapid light-off starts at ~200 °C and is accompanied with the highest selectivity to N₂. Then, around full conversion, N₂O becomes the main product and NO_x starts to form. With further heating, N₂O yield drops and NO_x yield gradually increases.

XANES regions of the QEXAFS spectra were analysed using Multivariate Curve Resolution (MCR), and three main spectral components were identified (fig. 7B), in line with the analysis of absorption of the white line shape (cf. fig. 6). The MCR-derived spectral components correspond to partially oxidized Pt with its white line intensity between Pt foil and PtO₂ (cf. fig. S30B). The obtained components were then used to perform the linear combination analysis (LCA) of the recorded spectra to track the interchange of Pt states in the course of the light-off.

The catalytic data acquired during the QEXAFS study was analysed along with the LCA results to correlate the catalyst performance to observed spectral features. Thus, the Pt L₃ spectra recorded at temperatures below light-off correspond to the first oxidized state, or the “low temperature component” of LCA in fig. 7B, C. The relative fraction of this component gradually declines with heating in the reaction mixture. The second, more reduced Pt state evolves with rise in temperature, marked as “middle temperature component” (fig. 7B, C.) As soon as its concentration exceeds the initial oxidized state concentration, light-off starts. The more reduced middle temperature state reaches its maximum around 100 % conversion and then decreases. The predominance of this component can be correlated to the high conversion and the highest selectivity to N₂. Shortly after complete conversion, platinum re-oxidised and another, high temperature oxidised component became predominant. It is denoted as “high temperature component” in fig. 7B, C. The prevalence of the oxidised high-temperature component over the reduced one is accompanied by N₂O becoming the main product. From this point, up to the maximum temperature tested, NO_x content in the products is gradually growing. Thus, the three spectral components detected with MCR correspond to three main

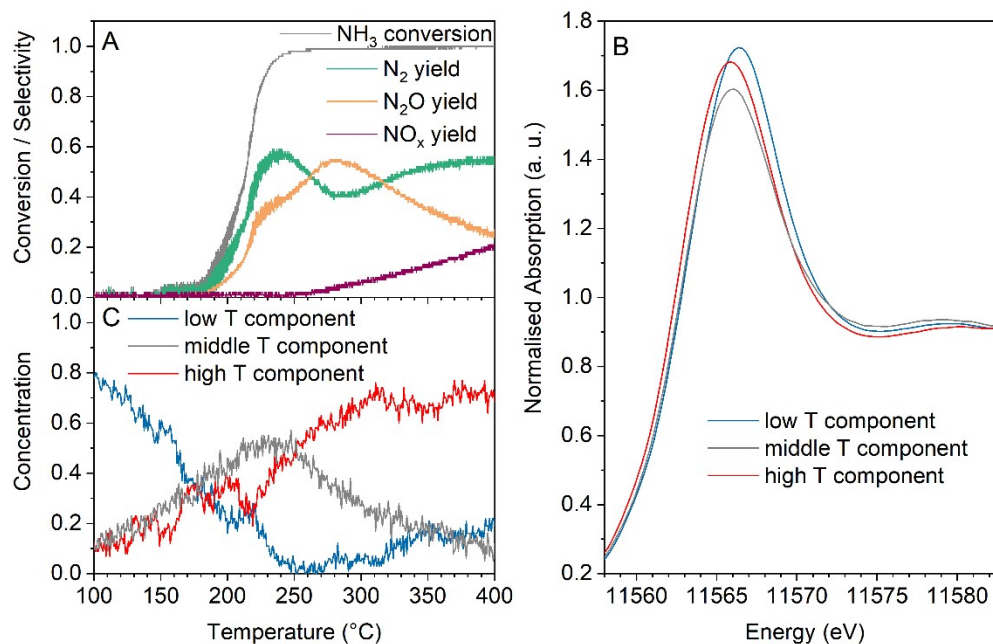


Figure 7. Results of *operando* QEXAFS analysis of PtA-IW-500 measured during a light-off in the reaction feed (500 ppm NH₃ and 10 % O₂ in inert). A – catalytic data; B – MCR-resolved spectral components from the QEXAFS dataset; C – evolution of relative fractions of the spectral components in the course of the light-off.



states of Pt during light-off that clearly correlate with its activity and selectivity. The surface species of Pt, from which the above-mentioned principal spectral components originate, should be further identified in future. This may help to deepen the understanding of the activity- and selectivity-governing factors and requires *operando* techniques complementary to XAS. The spectra obtained for the PtA-IW-700 were treated analogously to the PtA-IW-500 and showed similar, though less pronounced, trends. Like for the PtA-IW-500, three components with different white line shapes are observed in the *operando* QEXAFS spectra and shown in the contour plot in fig. S31. The white line intensity initially decreased with heating and then increased again at higher temperatures. The absorption maximum, as in the case of PtA-IW-500, slightly drifted to lower energies as the temperature increased. MCR analysis of PtA-IW-700 resolved three spectral components (fig. 8B), LCA-derived concentrations of which behave analogously to PtA-IW-500. The low-temperature component prevailing during the inactive phase of the catalytic cycle was again transformed to a more reduced middle-temperature component reaching its highest fraction with the highest N₂ yield. Finally, the third, high-temperature component is mostly observed during pronounced formation of the undesired N₂O and NO_x products. With all the similarities mentioned above, the difference between PtA-IW-700 and PtA-IW-500 is that the changes of the white line in the former catalyst are less pronounced. For example, change in the maximum absorption intensity in the MCR-resolved spectral components is ~0.15 (varies between ~1.6 and 1.75) for PtA-IW-500 containing Pt clusters, while this difference for the sample PtA-IW-700 with big nanoparticles constitutes only ~0.1 (varies between 1.3 and 1.4). The smaller white line differences also result in smaller concentration variations of the components. For the PtA-IW-500 they are ~0.1-

0.8, while for PtA-IW-700 – only ~0.2-0.5. These less distinct changes in the case of the sample with bigger particles can be explained with the fact that mainly surface Pt atoms participate in the reaction with bulk atoms being not much affected. In this way, the sample with smaller particles, that has a higher fraction of surface atoms, exhibit more pronounced changes in average state of platinum atoms that result in final XAS spectra. However, regardless of the different proportion of surface platinum atoms involved in the catalytic process, the similar white line changes evidence that the mechanism is the same for larger and smaller particles.

Zeolite-supported platinum. Analogous studies on zeolite-supported nanoparticles revealed the same trends as observed for alumina-supported clusters and nanoparticles with respect to the three principal spectral components and their correlation with catalyst performance. Contour plot of all light-off spectra for the PtZ-IW sample are shown in fig. S32. Similarly to the PtA-IW-500 and PtA-IW-700, PtZ-IW is first reduced during heating in the reaction mixture and then re-oxidized at elevated temperatures. A white line shift to lower energies for elevated-temperature spectral components can also be seen. The MCR algorithm, which was used for finding spectral components for the alumina-supported samples, failed to resolve sufficiently different spectral components in the present case. That is why, three most distinct spectra from fig. S32, also shown in fig. 9B, were used as spectral components to perform LCA of all other spectra measured for this catalyst. As fig. 9 shows, the low-temperature spectral shape (low-temperature component) is prevalent when the catalyst is inactive. Concentration increase of the second, middle temperature component, gives rise to the light-off. Like for the alumina-supported catalysts, it correlates with maximum N₂ selectivity when reaching full conversion. similar behaviour of the Pt L₃-spectra of Pt nanoparticles on

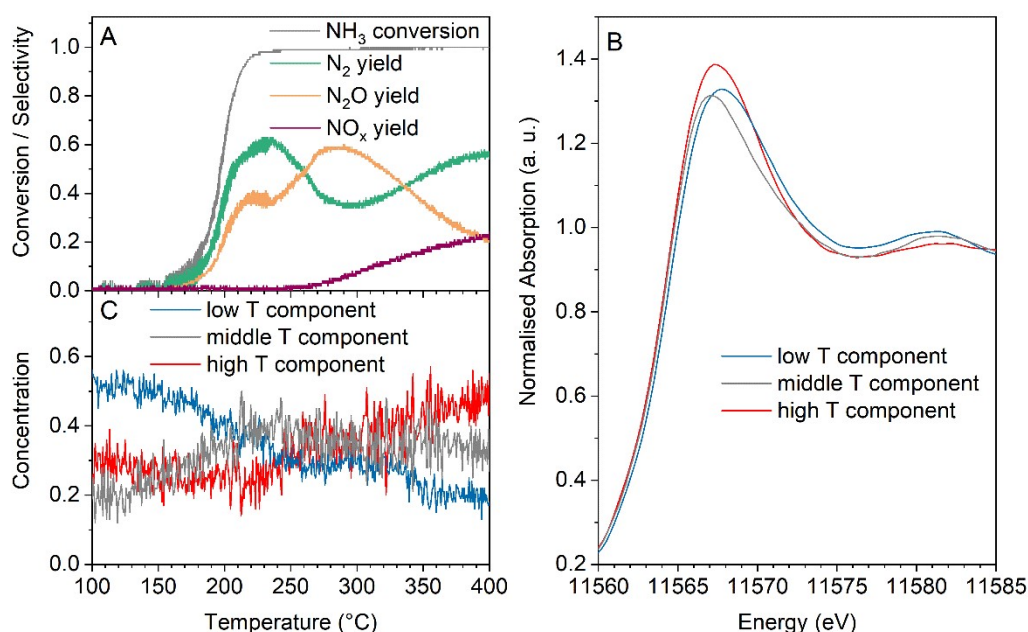


Figure 8. Results of *operando* QEXAFS analysis of PtA-IW-700 measured during a light-off in the reaction feed (500 ppm NH₃ and 10% O₂ in inert). A – catalytic data; B – MCR-resolved spectral components from the QEXAFS dataset; C – evolution of relative fractions of the spectral components in the course of the light-off.



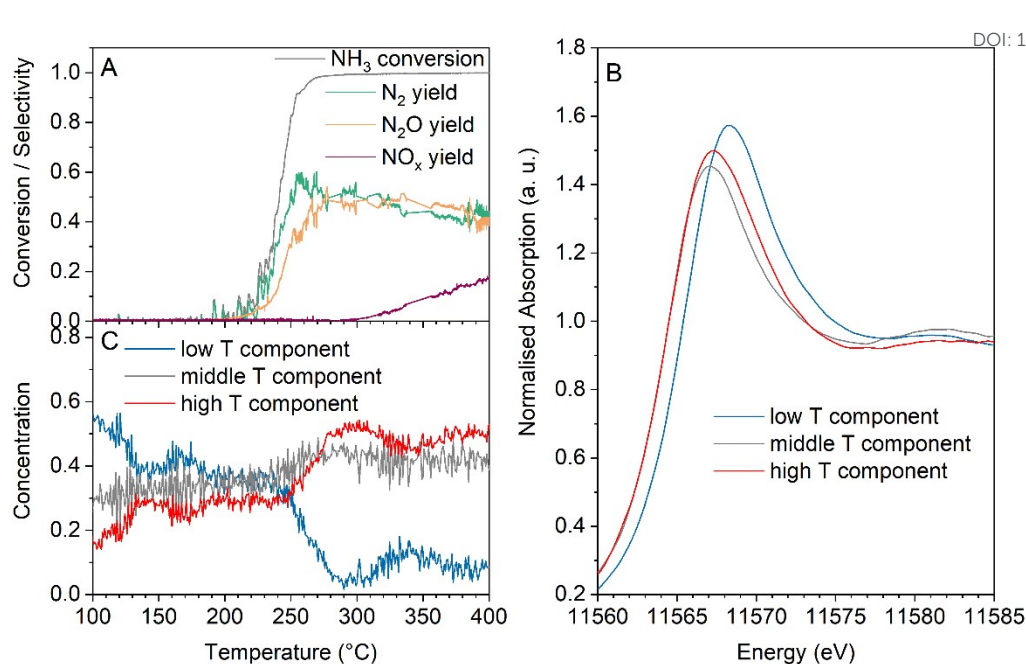


Figure 9. Results of operando QEXAFS analysis of PtZ-IW measured during a light-off in the reaction feed (1000 ppm NH₃ and 10 % O₂ in inert). A – catalytic data; B – spectral components for the QEXAFS dataset; C – evolution of relative fractions of the spectral components in the course of the light-off.

zeolite and the analogous correlation with catalytic performance we can conclude that the reaction occurs mainly on platinum according to the Ostwald process mechanism.

In contrast, the PtZ-IE containing mostly single Pt sites and small clusters demonstrated remarkably different spectral trends. Fig. 10 shows that the white line intensity of PtZ-IE decreased monotonously in the whole tested temperature range and did not undergo any combined reduction and reoxidation in the course of the light-off. Thus, only two different spectra can be resolved – the most oxidised catalyst at low temperature and the most reduced catalyst at high temperature. An absorption maximum shift to lower energies was also observed, as for other samples.

The main spectral components for *operando* QEXAFS data of PtZ-IE were found with MCR and their concentrations are juxtaposed with the catalytic data along the temperature axis in fig. 11. One spectral component prevails at low temperature with ~80 % concentration and decreases with temperature rise. The Pt state associated with it appears to be inactive, because the light-off starts very close to the point where the low-temperature component falls to less than half of the total content. The appearance of the high-temperature component was accompanied with an activity increase and also, to a large extent, monotonous growth of N₂ and NO_x (predominantly NO), which are the main products. This selectivity pattern is different from the one of nanoparticle/cluster-containing samples that include the stage of high N₂O yield. This observation, together with a different spectral behaviour, strongly evidences a different mechanism of ammonia oxidation on platinum single sites and small clusters.

In the section *catalytic tests* we already speculated that platinum single sites / small clusters are more likely to catalyse ammonia SCR than ammonia oxidation as the probability of ammonia dissociation on them is low. Based on our laboratory tests which show a very pronounced hysteresis, we assume that the presence of adsorbed species on the Pt sites inhibits the

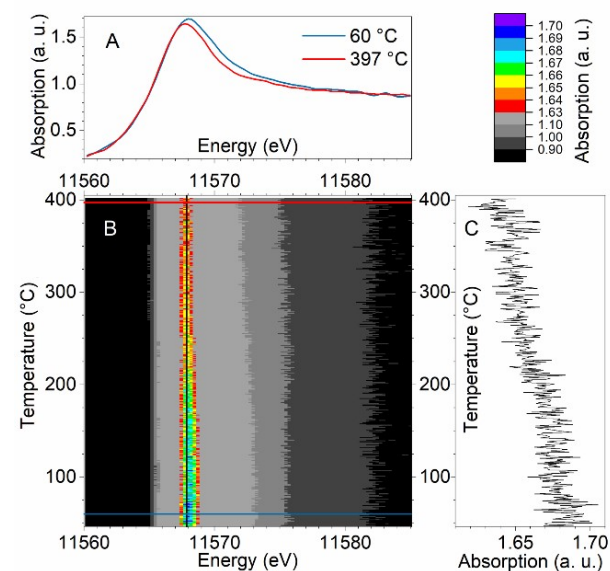


Figure 10. Contour plot of PtZ-IE or operando XANES spectra measured during the light-off in the reaction mixture (1000 ppm NH₃ and 10 % O₂ in inert). A – spectra with two most distinct white line shapes (energy profiles from the contour plot). B – the contour plot. C – absorption profile at the energy close to maximum absorption (11567.9 eV).



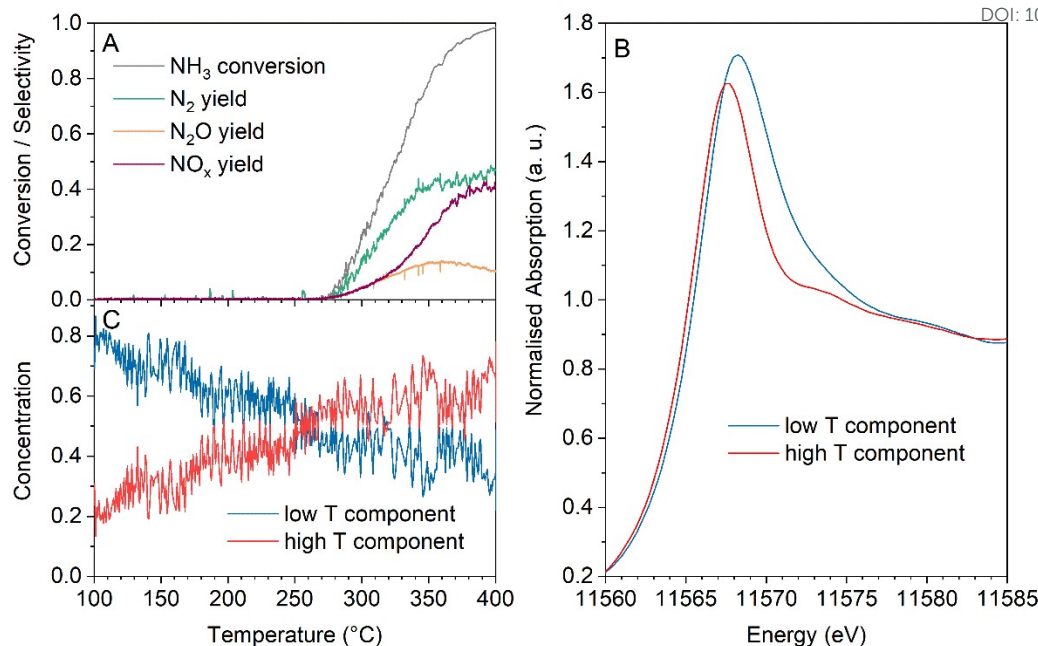


Figure 11. Results of *operando* QEXAFS analysis of PtZ-IE measured during a light-off in the reaction feed (1000 ppm NH₃ and 10 % O₂ in inert). A – catalytic data; B – MCR-resolved spectral components from the QEXAFS dataset; C – evolution of relative fractions of the spectral components in the course of the light-off.

catalytic activity at low temperatures. According to literature data, the inhibiting species could be either ammonia, which is a known poison for Fe and Cu SCR catalysts, or water which can compete for adsorption sites and alter the activity.^{83,84} From the reduction in the course of the light-off, it can be deduced that the low-temperature spectral component does not originate oxidation that produces some NO_x which further reacts with NH₃ by SCR on single sites and clusters.

Conclusions

To reveal factors governing the structural sensitivity in selective ammonia oxidation, laboratory tests and *operando* QEXAFS studies were conducted on well-characterised γ -Al₂O₃ and zeolite supported platinum catalysts with different particle sizes. The rate of ammonia activation rose with increasing particle size growing exponentially in the range of the smallest particles from single sites up to ~ 2 nm (fig. 12). In the nanometre size range, the activity rose more moderately demonstrating an almost linear but small gain with size increase. Hence, for an effective ammonia oxidation, particles of sufficient diameter are required that contain surface ensembles of Pt atoms needed for the activation step through oxygen-assisted ammonia dissociation, typical for the mechanism of ammonia oxidation in the Ostwald process. These ensembles are most probably B5 sites of Pt that can occur with a sufficient probability only on nanoparticles larger than ~ 2 nm. For larger particles, their fraction grows linearly, which corresponds to the observed linear increment of the reaction rate for particles larger than 2 nm (see fig. 12). In turn, Pt single sites and clusters, being below this threshold, exhibit lower

activity due to apparent constraints for the activation step. It is proposed that Pt particles in this size range rather catalyse SCR than ammonia oxidation. These conclusions are schematically summarised in fig. 12. The depicted trend was predicted theoretically³⁶ but has not been experimentally proven on supported catalysts under atmospheric pressures so far. The spectroscopic results further suggest a common mechanism for nanoparticle-containing samples, regardless of the support. Three surface Pt states correlating with catalyst performance were found for these catalysts. An initial oxidized state dominated at low temperatures while the catalyst was inactive. At intermediate temperatures the second, more reduced state (tentatively, clean nanoparticle surface) was prevalent and corresponded to the light-off and highest nitrogen yield. At high temperatures, the third state emerged that was oxidised again and was accompanied by high selectivity to N₂O and NO_x. Selectivity to nitrogen was generally higher for the less active samples, presumably due to slower removal of N-containing species from the surface. Zeolite-supported catalysts were generally more selective to N₂ because of their higher acidity and ammonia storage properties.

Constraints for the mechanism of ammonia oxidation on critically small Pt particles were confirmed spectroscopically for Pt single sites / small clusters on zeolite. This sample demonstrated only two main states with gradual change between the two states during the light-off, instead of a consecutive reduction and re-oxidation, as in the case of Pt nanoparticles.

In summary, the varying activity of Pt particles with their size increase can be used for tuning catalytic performance. Specifically, the use of catalysts with about 2 nm Pt particle size



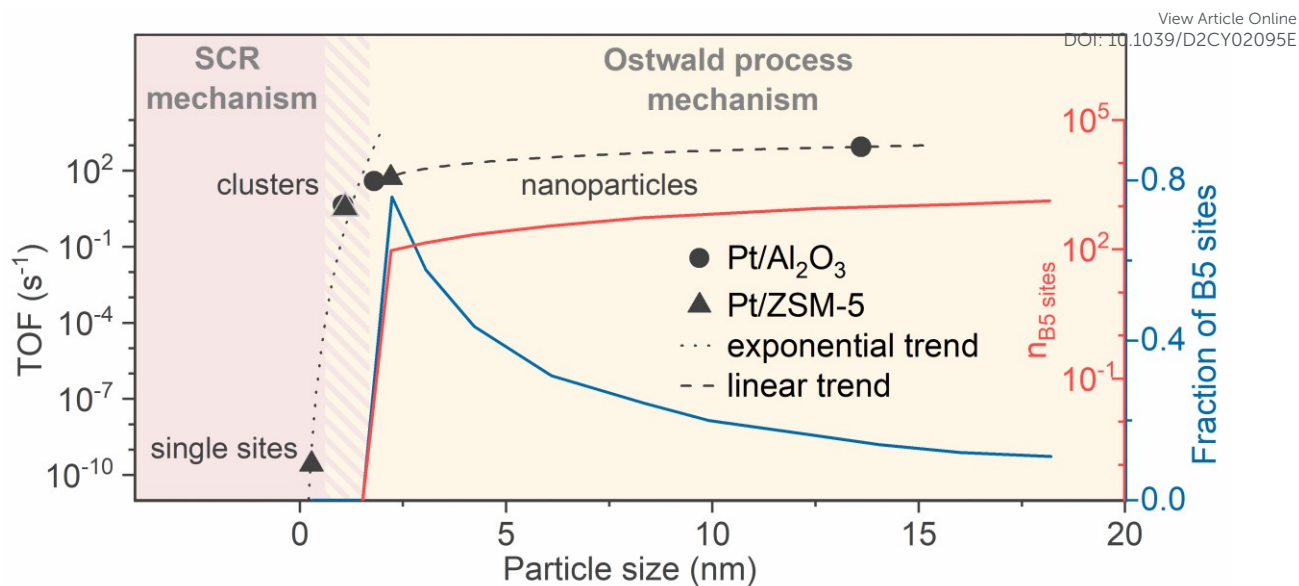


Figure 12. The dependence of the supported Pt catalysts' $T_{50\%}$ as well as of the fraction of B5 sites on Pt particle size. The fraction of B5 sites on Pt surface was plotted based on the results of G. A. Tritsarlis et al.⁷² and K. Honkala et al.⁷⁴ The number of B5 sites was estimated based on the relation of dispersion with particle size described on page S12 of SI and a dependence of number of atoms on particle size for a spherical particle of Pt described by A. Jentys.⁴⁹

can assure high concentration of active surface species necessary for efficient ammonia conversion. The impact of particle size on activity is substantially more significant than the impact of the studied supports. However, a support can be used as an additional variable to adjust catalytic properties. Thus, zeolite support increases catalyst selectivity and activity in dry feed; however, it leads to stronger deactivation in presence of water compared to alumina. Further identification of the states found in the platinum-containing catalysts and the surface species from which they originate is expected to deepen the understanding of the mechanism of this reaction and enable a more rational catalyst design.

Conflicts of interest

There are no conflicts to declare.

Acknowledgements

The work was funded by Helmholtz Initiative networking fund (HRSF-0046).

We acknowledge DESY (Hamburg, Germany), a member of the Helmholtz Association HGF, for the provision of experimental facilities. Parts of this research were carried out at PETRA III and we would like to thank Dr. Vadim Murzin (DESY), Dr. Wolfgang Caliebe and Dr. Benjamin Bornmann (BU Wuppertal, Germany) for assistance in using P64 beamline. Beamtimes were allocated for proposals I-20200270 and I-20181000. A further part of the XAS spectra for this research was measured at the CAT-ACT beamline of the KIT light source (Karlsruhe, Germany). We thank Dr. Anna Zimina for her support during the measurements.

The authors express their gratitude to Dr. Paolo Dolcet and Simon Barth (ITCP/IKFT, KIT) for their help during synchrotron measurements. We also thank Dr. Andrey I. Stadnichenko, Dr. Lidiya S. Kibis, Dr. Dmitry A. Svintsitskiy, and Dr. Andrei I. Boronin (Boreskov Institute of Catalysis) for their help during beamtimes, project planning and for valuable discussions.

The authors also acknowledge China Scholarship Council (CSC) for funding the PhD studies of Xiaohui Huang at the Karlsruhe Nano Micro Facility (KNMF) where the TEM data was recorded. We finally thank Dr. Di Wang (Institute of Nanotechnology, KIT) who supervised and assisted the TEM measurements.

References

- 1 A. Valera-Medina, H. Xiao, M. Owen-Jones, W. I. F. David and P. J. Bowen, *Prog. Energy Combust. Sci.*, 2018, **69**, 63-102.
- 2 Y. Kojima, *Int. J. Hydrog. Energy*, 2019, **44**, 18179-18192.
- 3 D. Miura and T. Tezuka, *Energy*, 2014, **68**, 428-436.
- 4 S. Giddey, S. P. S. Badwal, C. Munnings and M. Dolan, *ACS Sustain. Chem. Eng.*, 2017, **5**, 10231-10239.
- 5 N. Morlanes, S. P. Katikaneni, S. N. Paglieri, A. Harale, B. Solami, S. M. Sarathy and J. Gascon, *Chem. Eng. J.*, 2021, **408**, 127310.
- 6 T. Lan, Y. Zhao, J. Deng, J. Zhang, L. Shi and D. Zhang, *Catal. Sci. Technol.*, 2020, **10**, 5792-5810.
- 7 F. Gao, Y. Liu, Z. Sani, X. Tang, H. Yi, S. Zhao, Q. Yu and Y. Zhou, *J. Environ. Chem. Eng.*, 2021, **9**, 104575.
- 8 L. Chmielarz and M. Jabłońska, *RSC Adv.*, 2015, **5**, 43408-43431.
- 9 M. Colombo, I. Nova and E. Tronconi, *Catal. Today*, 2012, **197**, 243-255.
- 10 P. S. Dhillon, M. P. Harold, D. Wang, A. Kumar and S. Y. Joshi, *Chem. Eng. J.*, 2019, **377**, 119734.
- 11 A. Scheuer, A. Drochner, J. Gieshoff, H. Vogel and M. Votsmeier, *Catal. Today*, 2012, **188**, 70-79.



- 12 A. Scheuer, W. Hauptmann, A. Drochner, J. Gieshoff, H. Vogel and M. Votsmeier, *Appl. Catal. B*, 2012, **111-112**, 445-455.
- 13 P. S. Dhillon, M. P. Harold, D. Wang, A. Kumar and S. Joshi, *Catal. Today*, 2019, **320**, 20-29.
- 14 R. Imbihl, A. Scheibe, Y. F. Zeng, S. Günther, R. Kraehnert, V. A. Kondratenko, M. Baerns, W. K. Offermans, A. P. J. Jansen and R. A. van Santen, *Phys. Chem. Chem. Phys.*, 2007, **9**, 3522-3540.
- 15 A. Scheibe, U. Lins and R. Imbihl, *Surf. Sci.*, 2005, **577**, 1-14.
- 16 J. Pérez-Ramírez, E. V. Kondratenko, G. Novell-Leruth and J. M. Ricart, *J. Catal.*, 2009, **261**, 217-223.
- 17 R. Kraehnert and M. Baerns, *Appl. Catal. A: Gen.*, 2007, **327**, 73-81.
- 18 M. Baerns, R. Imbihl, V. A. Kondratenko, R. Kraehnert, W. K. Offermans, R. A. van Santen and A. Scheibe, *J. Catal.*, 2005, **232**, 226-238.
- 19 J. Schäffer, V. A. Kondratenko, N. Steinfeldt, M. Sebek and E. V. Kondratenko, *J. Catal.*, 2013, **301**, 210-216.
- 20 Y. F. Zeng and R. Imbihl, *J. Catal.*, 2009, **261**, 129-136.
- 21 D. P. Sobczyk, E. J. M. Hensen, A. M. de Jong and R. A. van Santen, *Top. Catal.*, 2003, **23**, 109-117.
- 22 Y. Li and J. N. Armor, *Appl. Catal. B*, 1997, **13**, 131-139.
- 23 A. M. Gänzler, B. Betz, S. Baier-Stegmaier, S. Belin, V. Briois, M. Votsmeier and M. Casapu, *J. Phys. Chem. C*, 2020, **124**, 20090-20100.
- 24 D. Decarolis, A. H. Clark, T. Pellegrinelli, M. Nachtegaal, E. W. Lynch, C. R. A. Catlow, E. K. Gibson, A. Goguet and P. P. Wells, *ACS Catal.*, 2021, **11**, 2141-2149.
- 25 G. A. Somorjai, K. R. McCrea and J. Zhu, *Top. Catal.*, 2002, **18**, 157-166.
- 26 J. J. Ostermaier, J. R. Katzer and W. H. Manogue, *J. Catal.*, 1974, **33**, 457-473.
- 27 J. J. Ostermaier, J. R. Katzer and W. H. Manogue, *J. Catal.*, 1976, **41**, 277-292.
- 28 A. C. M. van den Broek, J. van Grondelle and R. A. van Santen, *J. Catal.*, 1999, **185**, 297-306.
- 29 A. C. M. van den Broek, DOI: 10.6100/IR517149, PhD Thesis, Eindhoven University of Technology, 1998.
- 30 E. M. Slavinskaya, L. S. Kibis, O. A. Stonkus, D. A. Svintsitskiy, A. I. Stadnichenko, E. A. Fedorova, A. V. Romanenko, V. Marchuk, D. E. Doronkin and A. I. Boronin, *ChemCatChem*, 2021, **13**, 313-327.
- 31 T. K. Hansen, <https://orbit.dtu.dk/en/publications/development-of-new-diesel-oxidation-and-nhsub3sub-slip-catalysts>, PhD thesis, Technical University of Denmark, 2017.
- 32 L. S. Kibis, D. A. Svintsitskiy, A. I. Stadnichenko, E. M. Slavinskaya, A. V. Romanenko, E. A. Fedorova, O. A. Stonkus, V. A. Svetlichnyi, E. D. Fakhruddinova, M. Vorokhta, B. Smid, D. E. Doronkin, V. Marchuk, J.-D. Grunwaldt and A. I. Boronin, *Catal. Sci. Technol.*, 2021, **11**, 250-263.
- 33 D. A. Svintsitskiy, L. S. Kibis, A. I. Stadnichenko, E. M. Slavinskaya, A. V. Romanenko, E. A. Fedorova, O. A. Stonkus, D. E. Doronkin, V. Marchuk, A. Zimina, M. Casapu, J.-D. Grunwaldt and A. I. Boronin, *ChemCatChem*, 2020, **12**, 867-880.
- 34 M. Machida, Y. Tokudome, A. Maeda, Y. Kuzuhara, T. Hirakawa, T. Sato, H. Yoshida, J. Ohyama, K. Fujii and N. Ishikawa, *ACS Catal.*, 2020, **10**, 4677-4685.
- 35 M. Casapu, A. Fischer, A. M. Gänzler, R. Popescu, M. Crone, D. Gerthsen, M. Turk and J.-D. Grunwaldt, *ACS Catal.*, 2017, **7**, 343-355.
- 36 R. A. van Santen, *Acc. Chem. Res.*, 2009, **42**, 57-66.
- 37 G. T. Whiting, F. Meirer and B. M. Weckhuysen, in *XAFS Techniques for Catalysts, Nanomaterials, and Surfaces*, eds. Y. Iwasawa, K. Asakura and M. Tada, Springer International Publishing, Cham, 2017, DOI: 10.1007/978-3-319-43866-5_13, pp. 167-191.
- 38 B. B. Sarma, F. Maurer, D. E. Doronkin and J.-D. Grunwaldt, *Chem. Rev.*, 2022, DOI: 10.1021/acs.chemrev.2c00495.
- 39 A. Boubnov, S. Dahl, E. Johnson, A. P. Molina, S. B. Simonsen, F. M. Cano, S. Helveg, L. J. Lemus-Yegres and J.-D. Grunwaldt, *Appl. Catal. B*, 2012, **126**, 315-325.
- 40 A. Philippaerts, S. Paulussen, S. Turner, O. I. Lebedev, G. van Tendeloo, H. Poelman, M. Bulut, F. de Clippel, P. Smeets, B. Sels and P. Jacobs, *J. Catal.*, 2010, **270**, 172-184.
- 41 A. C. M. van den Broek, J. van Grondelle and R. A. van Santen, *J. Catal.*, 1997, **167**, 417-424.
- 42 M. Abramoff, P. Magalhães and S. J. Ram, *Biophotonics Int.*, 2003, **11**, 36-42.
- 43 A. Zimina, K. Dardenne, M. A. Denecke, D. E. Doronkin, E. Huttel, H. Lichtenberg, S. Mangold, T. Pruessmann, J. Rothe, T. Spangenberg, R. Steininger, T. Vitova, H. Geckeis and J.-D. Grunwaldt, *Rev. Sci. Instrum.*, 2017, **88**, 113113.
- 44 B. Ravel and M. Newville, *J. Synchrotron Radiat.*, 2005, **12**, 537-541.
- 45 C. Baerlocher, W. M. Meier and D. H. Olson, in *Atlas of Zeolite Framework Types*, Elsevier, Amsterdam, The Netherlands, 5th edn., 2001, pp. 184-185.
- 46 B. F. Mentzen and G. Bergeret, *J. Phys. Chem. C*, 2007, **111**, 12512-12516.
- 47 A. H. Clark, J. Imbao, R. Frahm and M. Nachtegaal, *J. Synchrotron Radiat.*, 2020, **27**, 551-557.
- 48 J.-D. Grunwaldt, M. Caravati, S. Hannemann and A. Baiker, *Phys. Chem. Chem. Phys.*, 2004, **6**, 3037-3047.
- 49 A. Jentys, *Phys. Chem. Chem. Phys.*, 1999, **1**, 4059-4063.
- 50 P. V. Menacherry and G. L. Haller, *Catal. Lett.*, 1997, **44**, 135-144.
- 51 K. Chakarova, M. Mihaylov and K. Hadjiivanov, *Microporous Mesoporous Mater.*, 2005, **81**, 305-312.
- 52 Y. Li, M. Kottwitz, J. L. Vincent, M. J. Enright, Z. Liu, L. Zhang, J. Huang, S. D. Senanayake, W.-C. D. Yang, P. A. Crozier, R. G. Nuzzo and A. I. Frenkel, *Nat. Commun.*, 2021, **12**, 914.
- 53 M. A. Newton, D. Ferri, G. Smolentsev, V. Marchionni and M. Nachtegaal, *J. Am. Chem. Soc.*, 2016, **138**, 13930-13940.
- 54 L. M. Kustov, D. Ostgard and W. M. H. Sachtler, *Catal. Lett.*, 1991, **9**, 121-126.
- 55 T. J. Toops, D. B. Smith, W. S. Epling, J. E. Parks and W. P. Partridge, *Appl. Catal. B*, 2005, **58**, 255-264.
- 56 A. Y. Stakheev, E. S. Shpiro, O. P. Tkachenko, N. I. Jaeger and G. Schulz-Ekloff, *J. Catal.*, 1997, **169**, 382-388.
- 57 K. Ding, A. Gulec, A. M. Johnson, N. M. Schweitzer, G. D. Stucky, L. D. Marks and P. C. Stair, *Science*, 2015, **350**, 189.
- 58 L. DeRita, S. Dai, K. Lopez-Zepeda, N. Pham, G. W. Graham, X. Pan and P. Christopher, *J. Am. Chem. Soc.*, 2017, **139**, 14150-14165.
- 59 J. Jones, H. Xiong, A. T. DeLaRiva, E. J. Peterson, H. Pham, S. R. Challa, G. Qi, S. Oh, M. H. Wiebenga, X. I. Pereira Hernández, Y. Wang and A. K. Datye, *Science*, 2016, **353**, 150.
- 60 F. C. Meunier, *J. Phys. Chem. C*, 2021, **125**, 21810-21823.
- 61 F. Maurer, J. Jelic, J. Wang, A. Gänzler, P. Dolcet, C. Wöll, Y. Wang, F. Studt, M. Casapu and J.-D. Grunwaldt, *Nat. Catal.*, 2020, **3**, 824-833.
- 62 H. Wang, J.-X. Liu, L. F. Allard, S. Lee, J. Liu, H. Li, J. Wang, J. Wang, S. H. Oh, W. Li, M. Flytzani-Stephanopoulos, M. Shen, B. R. Goldsmith and M. Yang, *Nat. Commun.*, 2019, **10**, 3808.
- 63 J. D. Kistler, N. Chotigkrai, P. Xu, B. Enderle, P. Praserthdam, C.-Y. Chen, N. D. Browning and B. C. Gates, *Angew. Chem. Int. Ed.*, 2014, **53**, 8904-8907.



ARTICLE

Journal Name

- 64 A. Kaftan, F. Kollhoff, T.-S. Nguyen, L. Piccolo, M. Laurin and J. Libuda, *Catal. Sci. Technol.*, 2016, **6**, 818-828.
- 65 Q. Xu, B. T. Heaton, C. Jacob, K. Mogi, Y. Ichihashi, Y. Souma, K. Kanamori and T. Eguchi, *J. Am. Chem. Soc.*, 2000, **122**, 6862-6870.
- 66 B. P. Andreini, D. Belli Dell'Amico, F. Calderazzo, M. G. Venturi, G. Pelizzi and A. Serge, *J. Organomet. Chem.*, 1988, **354**, 357-368.
- 67 K. Feng, H. Z. Zhang, J. Gao, J. B. Xu, Y. M. Dong, Z. H. Kang and J. Zhong, *Appl. Phys. Lett.*, 2020, **116**, 191903
- 68 G. Novell-Leruth, A. Valcárcel, A. Clotet, J. M. Ricart and J. Pérez-Ramírez, *J. Phys. Chem. B*, 2005, **109**, 18061-18069.
- 69 R. S. Ghosh, P. S. Dhillon, M. P. Harold and D. Wang, *Chem. Eng. J.*, 2021, **417**, 128273.
- 70 H. Ma and W. F. Schneider, *ACS Catal.*, 2019, **9**, 2407-2414.
- 71 A. S. Ramachandran, S. L. Anderson and A. K. Datye, *Ultramicroscopy*, 1993, **51**, 282-297.
- 72 G. A. Tritsarlis, J. Greeley, J. Rossmeis and J. K. Nørskov, *Catal. Lett.*, 2011, **141**, 909-913.
- 73 R. van Hardeveld and A. van Montfoort, *Surf. Sci.*, 1966, **4**, 396-430.
- 74 K. Honkala, A. Hellman, I. N. Remediakis, A. Logadottir, A. Carlsson, S. Dahl, C. H. Christensen and J. K. Nørskov, *Science*, 2005, **307**, 555-558.
- 75 J. Pérez-Ramírez, E. V. Kondratenko, V. A. Kondratenko and M. Baerns, *J. Catal.*, 2005, **229**, 303-313.
- 76 J. Pérez-Ramírez, E. V. Kondratenko, V. A. Kondratenko and M. Baerns, *J. Catal.*, 2004, **227**, 90-100.
- 77 O. Ivashenko, N. Johansson, C. Pettersen, M. Jensen, J. Zheng, J. Schnadt and A. O. Sjøstad, *ACS Catal.*, 2021, **11**, 8261-8273.
- 78 J. D. Gonzalez, K. Shojaee, B. S. Haynes and A. Montoya, *Phys. Chem. Chem. Phys.*, 2018, **20**, 25314-25323.
- 79 C. Wang, D. Ren, G. Harle, Q. Qin, L. Guo, T. Zheng, X. Yin, J. Du and Y. Zhao, *J. Hazard. Mater.*, 2021, **416**, 125782.
- 80 M. M. Sun, S. N. Wang, Y. S. Li, Q. Wang, H. D. Xu and Y. Q. Chen, *J. Taiwan Inst. Chem. Eng.*, 2017, **78**, 401-408.
- 81 T. Yu, M. Xu, Y. Huang, J. Wang, J. Wang, L. Lv, G. Qi, W. Li and M. Shen, *Appl. Catal. B*, 2017, **204**, 525-536.
- 82 A. Boubnov, H. W. P. Carvalho, D. E. Doronkin, T. Günter, E. Gallo, A. J. Atkins, C. R. Jacob and J.-D. Grunwaldt, *J. Am. Chem. Soc.*, 2014, **136**, 13006-13015.
- 83 B. Kerkeni, D. Berthout, D. Berthomieu, D. E. Doronkin, M. Casapu, J.-D. Grunwaldt and C. Chizallet, *J. Phys. Chem. C*, 2018, **122**, 16741-16755.
- 84 A. R. Fahami, T. Gunter, D. E. Doronkin, M. Casapu, D. Zengel, T. H. Vuong, M. Simon, F. Breher, A. V. Kucherov, A. Brückner and J.-D. Grunwaldt, *React. Chem. Eng.*, 2019, **4**, 1000-1018.
- 85 H. Wang, M. Lin, T. Murayama, S. Feng, M. Haruta, H. Miura and T. Shishido, *J. Catal.*, 2021, **402**, 101-113.
- 86 M. Y. Lin, B. X. An, T. Takei, T. Shishido, T. Ishida, M. Haruta and T. Murayama, *J. Catal.*, 2020, **389**, 366-374.
- 87 J. Singh, E. M. C. Alayon, M. Tromp, O. V. Safonova, P. Glatzel, M. Nachtegaal, R. Frahm and J. A. van Bokhoven, *Angew. Chem. Int. Ed.*, 2008, **47**, 9260-9264.
- 88 H. Yoshida, S. Nonoyama, Y. Yazawa and T. Hattori, *Phys. Scr.*, 2005, **T115**, 813-815.
- 89 Y. Lei, J. Jelic, L. C. Nitsche, R. Meyer and J. Miller, *Top. Catal.*, 2011, **54**, 334-348.

View Article Online
DOI: 10.1039/D2CY02095E

